NASA TECHNICAL NOTE

NASA TN D-2756

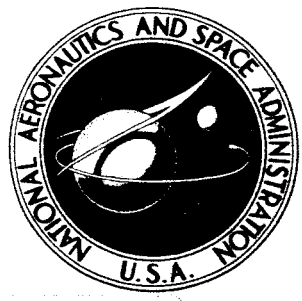

NASA TN D-2756

FLIGHT PERFORMANCE DATA FROM THE SCOUT X-258 ROCKET MOTOR

by James A. Nagy

Goddard Space Flight Center

Greenbelt, Md.

NATIONAL AERONAUTICS AND SPACE ADMINISTRATION • WASHINGTON, D. C. • MAY 1965

NASA TN D-2756

FLIGHT PERFORMANCE DATA FROM THE SCOUT X-258 ROCKET MOTOR

By James A. Nagy

Goddard Space Flight Center
Greenbelt, Md.

NATIONAL AERONAUTICS AND SPACE ADMINISTRATION

For sale by the Clearinghouse for Federal Scientific and Technical Information
Springfield, Virginia 22151 – Price $3.00

FLIGHT PERFORMANCE DATA FROM THE SCOUT X-258 ROCKET MOTOR

by
James A. Nagy
Goddard Space Flight Center

SUMMARY

23160

Nine channels of performance data were obtained during the flight of the Scout launch vehicle (S-122) on December 19, 1963. This vehicle was used to place the Langley Research Center satellite Explorer XIX into earth orbit from Point Arguello, California.

Shock and vibration data were obtained from the forward motor shoulder (payload attach point) of the fourth stage X-258 from liftoff through fourth-stage motor burnout. Low-level random vibrations (below 0.0016 g^2/cps) were recorded during first-stage burning and are the subject of detailed analysis in this report. First-stage motor burning irregularities which caused increases in vibration level at the payload also are analyzed, as well as transients recorded during first- and third-stage burning. No appreciable vibrations were apparent during fourth-stage burning; this correlates with results obtained during a simulated high-altitude static firing of an X-258. There was no indication of X-258 chuffing; however, the tailoff was exceedingly long.

Low-frequency accelerometers included in the experiment measured lateral bending frequencies and low-frequency vehicle pitching and yawing motions during the first three stages of burning. Spin rate and gyroscopic motions during fourth-stage burning were recorded, as well as axial steady-state acceleration for all four stages. The experiment also measured X-258 headcap pressure. The X-258 forward dome temperature is presented for the first 2 hours after fourth-stage ignition.

CONTENTS

FLIGHT PERFORMANCE DATA FROM THE SCOUT X-258 ROCKET MOTOR

by
James A. Nagy
Goddard Space Flight Center

INTRODUCTION

The development program of the NASA Langley Research Center to improve the performance of the Scout launch vehicle has led to a new fourth-stage solid rocket motor, the X-258. Instrumented ground firings at sea level and at simulated high altitude have shown that the X-258 exhibits no oscillatory burning and that practically no vibrations exist at the X-258 payload attach point.*

To confirm the static firing results and to establish laboratory vibration test specifications for X-258 payloads, it was considered necessary to measure the in-flight vibrations. Prior to this, no in-flight measurements had been made on the X-258. In addition to the vibration measurements, transducers were included in the experiment to measure the following X-258 performance parameters: steady accelerations, spin rate, temperature, headcap pressure, tipoff, coning, and chuffing. The experiment also telemetered a signal to verify that the spacecraft separation sequence of events had occurred.

The performance experiment was implemented by Goddard Space Flight Center (GSFC) at the request of Langley Research Center as a secondary experiment. The primary experiment was the Langley Air Density Satellite, Explorer XIX (1963 53A). The Scout vehicle (S-122) was launched by the Air Force Space Systems Division from the Probe Launch Complex, Naval Missile Facility, Point Arguello, California, on December 19, 1963. The vehicle followed a nominal trajectory and placed the satellite in an earth orbit.

The purpose of this report is to present the in-flight shock and vibration data. Although data from the other transducers are presented, no attempt is made to analyze X-258 or Scout vehicle performance.

As a reference for the data, the vehicle is described and typical time histories of flight performance, as well as the times of significant events, are presented.

*See Tereniak, W. B., "X-258 Development Motor Static Firing Vibration Data," Goddard Space Flight Center Memorandum Report 631-184, December 4, 1963. It should be noted that the X-258's predecessor, the X-248, did exhibit oscillatory burning.

DESCRIPTION OF THE VEHICLE AND PAYLOAD

The Scout vehicle is a 72-foot, multistage, solid fuel research missile developed by Langley Research Center (Figure 1).

Four solid rocket motors are joined by airframe assemblies called transition sections. Additional airframe assemblies include a base section, heat shield, and wiring tunnels. Each transition section is divided into upper and lower portions at the stage separation plane. Frangible "blowout" diaphragms join the *first and second* and the *second and third* stages. The diaphragms form an internal clamp by the threaded periphery that engages two structural threaded rings at the separation plane. Blast pressure of the upstage motor ruptures the diaphragm, disengages the periphery, and allows the stage to separate. The third and fourth stages are joined by a "cold-separation" arrangement of springs held compressed by a clamp retainer flange. Explosive bolt clamps release the flanges, effecting separation by spring-loaded ejection force.

Base section A, shown in Figure 2, contains electrohydraulic actuators used to control a combination of jet vanes and aerodynamic tip control surfaces for guidance control

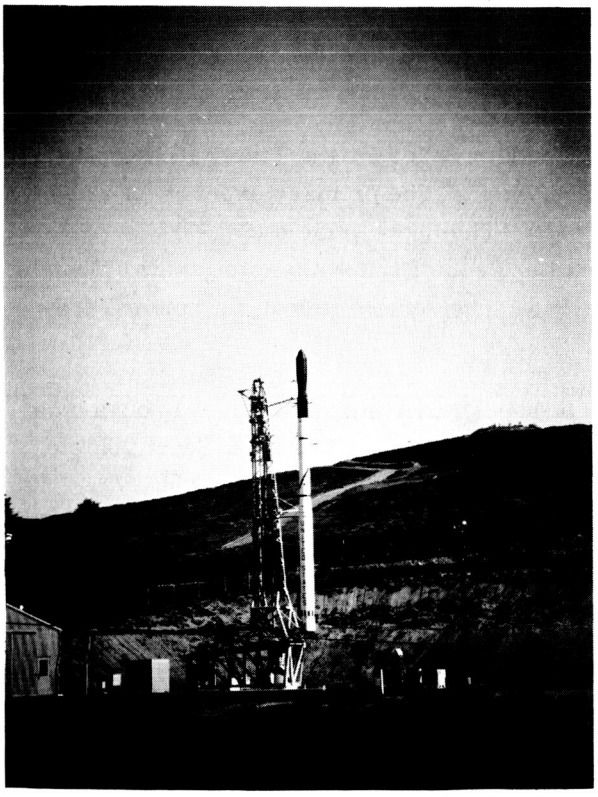

Figure 1—The Scout vehicle on its launch pad.

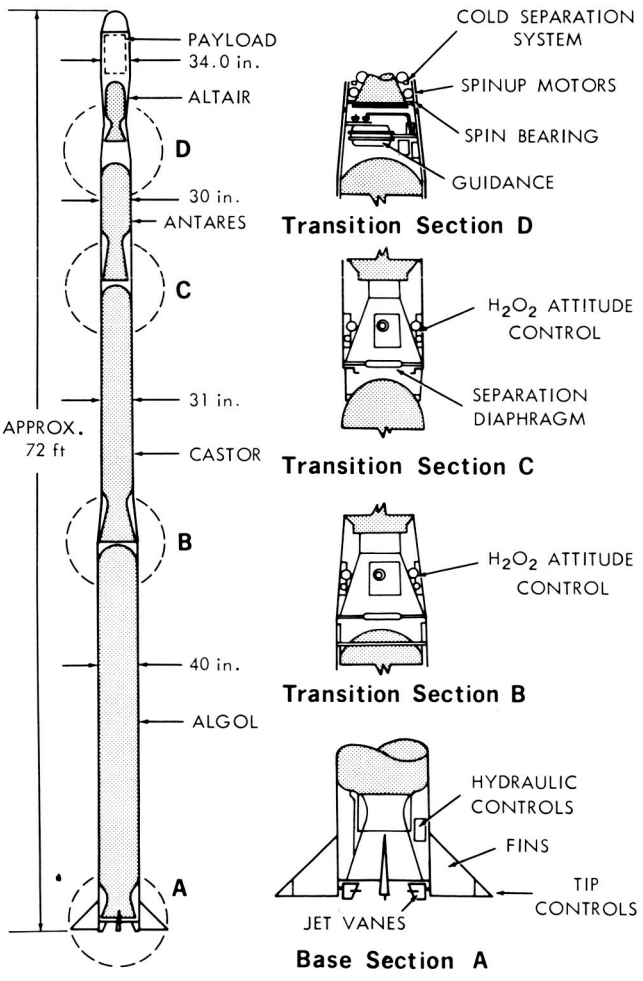

Figure 2—General arrangement of vehicle.

throughout the entire first-stage burning period. Transition B section (between first and second stage) and transition C section (between second and third stage) contain second- and third-stage control systems of hydrogen peroxide reaction jet motors. Transition lower D section contains the guidance system and the fourth-stage spinup system. Transition upper D section, where the performance experiment antennas are located, is attached to the fourth-stage aft motor shoulder.

The payload, consisting of four sections, was attached to the forward motor shoulder of the X-258 as depicted in Figures 3 and 4. The lower extension contains a beacon transmitter and its antennas, payload umbilical, and piezoelectric accelerometers. The upper extension contains four low-frequency accelerometers and the performance telemeter. Satellite timers and batteries for pyrotechnics are located on the frustum, and attached to the frustum is a canister which accommodates the folded 12-foot-diameter inflatable satellite.

A 34-inch-diameter clamshell-type heat shield protects the payload during ascent. The heat shield is ejected when the vehicle is out of the sensible atmosphere by latch-contained springs, after release of latches and clamps effected by a ballistic actuator and drawbar.

The total payload weight, including ballast, amounted to 138.50 pounds.

Changes made in the vehicle for this flight were: (1) The first stage had a modified

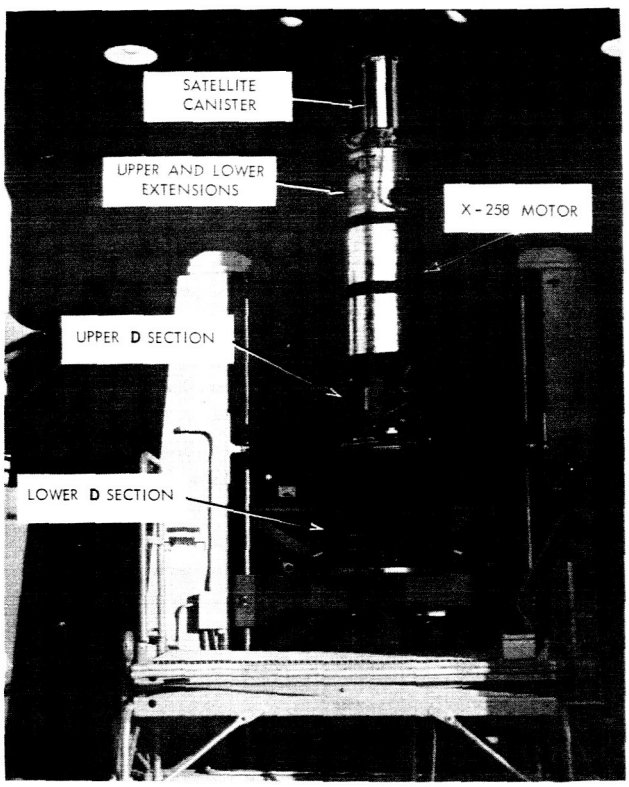

Figure 3—Fourth-stage arrangement.

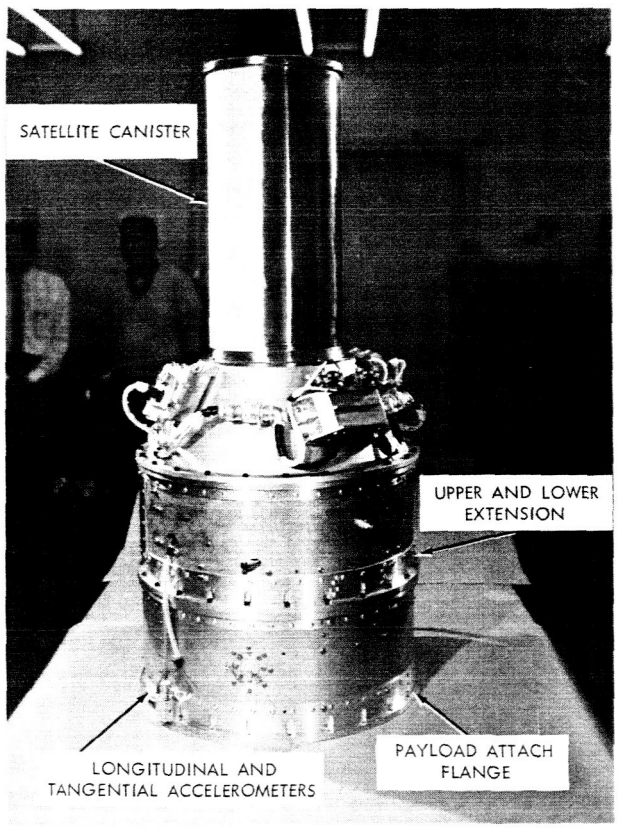

Figure 4—Payload configuration.

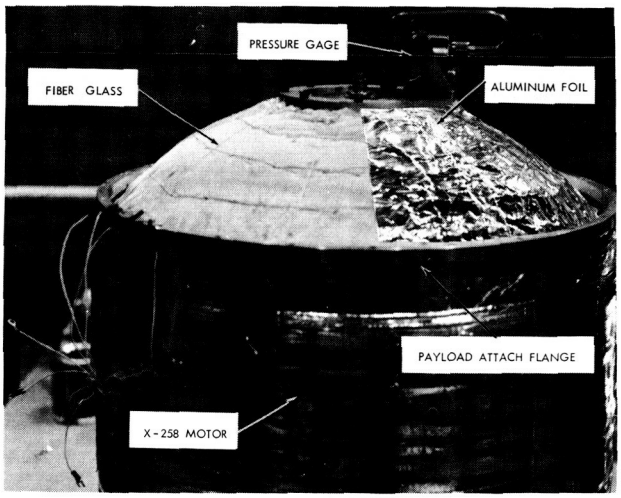

Figure 5–X-258 forward dome blanket (shown partially installed).

Algol IIA nozzle; (2) a heat shield was installed in transition upper C section to reduce heat transferred from the X-259 motor nozzle to the hydrogen peroxide system, and insulation was added in localized areas to further protect the system; (3) additional instrumentation was installed in C section to provide more performance and environmental data on the control system; (4) the X-258 rocket motor case was overwrapped with 0.20-inch-thick filament; and (5) the X-258 dome was covered with an insulating blanket for thermal protection of the performance experiment, as shown in Figure 5.

Table 1 lists the nominal dimensions and predicted performance characteristics of the four motors.

Table 1

Nominal Dimensional and Predicted Performance Characteristics of the Four Rocket Motors

Characteristics	Stage I Algol IIA S/N 21	Stage II Castor XM33-E5 S/N 152	Stage III Antares X259-A3 S/N HPC-134	Stage IV Altair X258-B1 S/N RH 61
Motor temperature (°F)	70	70	70	70
Overall length (in.)	357.6	244.1	113.7	58.4
Principal diameter (in.)	40.0	31.0	30.05	18.05
Propellant weight (lb)	21,087	7,326	2,580	504.8
Loaded motor weight (lb)	23,583	8,867	2,818	574.5
Burnout motor weight (lb)	2,212	1,435	*213	63.3
Consumed weight (lb)	21,371	7,432	2,605	511.2
Propellant specific impulse, vacuum (lb -sec/lb_w)	258.29	273.21	278.72	281.88
Total impulse, vacuum (lb-sec)	5,446,605	2,001,536	719,098	142,292
Average thrust, based on total burntime (lb)	79,862.2	47,106.1	21,529.9	5472.8
Total burntime (sec)	68.2	42.49	33.4	26.0
Nozzle expansion ratio	7.32	15.61	17.93	25.80
Exit area (sq ft)	5.648	8.083	4.346	1.367

*This weight includes 13.8 lb Thermolag, 8 lb of which is consumed during first- and second-stage operation.

INSTRUMENTATION

To determine the primary experimental objective of X-258 motor performance, the experiment was installed in the upper extension illustrated in Figure 6. Sensors were installed in the payload area to measure vibration, acceleration, spin rate, tipoff, X-258 dome temperature, X-258

Table 2

Performance Experiment Channel Assignments
(Transmission frequency, 240.2 Mc)

IRIG Channel	Center Frequency (kc)	Instrument and Function	Instrument Range (nominal)
E	70.0	Vibration - longitudinal, forward motor shoulder	$\pm 14g = 1.61\ v_{rms}$ at 100 cps
C	40.0	Vibration - tangential, forward motor shoulder	$\pm 14g = 1.61\ v_{rms}$ at 100 cps
A	22.0	Vibration - radial, forward motor shoulder	$\pm 14g = 1.61\ v_{rms}$ at 100 cps
12	10.5	Acceleration - longitudinal	$^{+36}_{-2g} = 131$ Mv/g
11	7.35	Acceleration - longitudinal	$\pm 1/2g$
10	5.4	Acceleration - pitch + spin	$\pm 1g$
9	3.9	Acceleration - yaw	$\pm 1g$
8	3.0	X-258 motor headcap pressure	0-485 lb/sq in. abs
7	2.3	X-258 motor dome temperature	0-1000°F
6	1.7	Air Density Explorer events	0-5v

heatcap pressure, and chuffing. Figure 7 gives the locations of the transducers. Table 2 shows the instrument range and telemeter channel assignments.

Signals from the transducers were conditioned and fed into an FM/FM 2-watt telemeter as shown by block diagram in Figure 8. The RF signal was transmitted via quadraloop antennas mounted on upper D section and recorded at Pacific Missile Range (PMR) and NASA ground stations. Magnetic tape records of the composite FM data, obtained from NASA ground stations at Point Arguello and San Diego and from PMR stations at Pretoria, Africa; South Point, Hawaii; and the down-range ship Richfield were reduced.

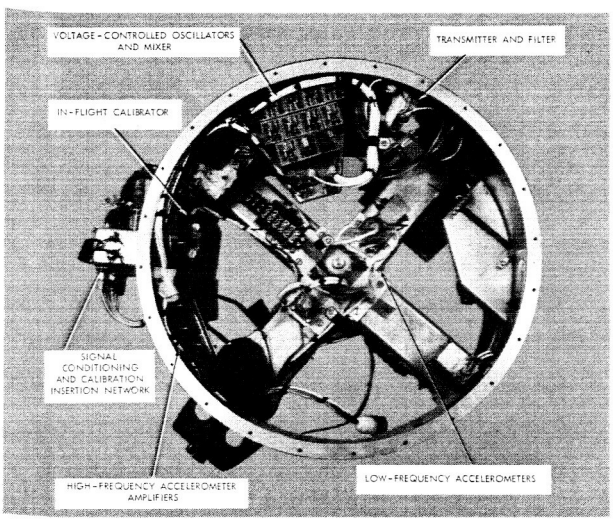

Figure 6—Upper payload extension (shown assembled).

DATA REDUCTION

The magnetic tape records received from the ground stations were reduced at GSFC with the system shown in Figure 9.

Data reduction consisted of

1. "Quick look" to determine the nature of the data,

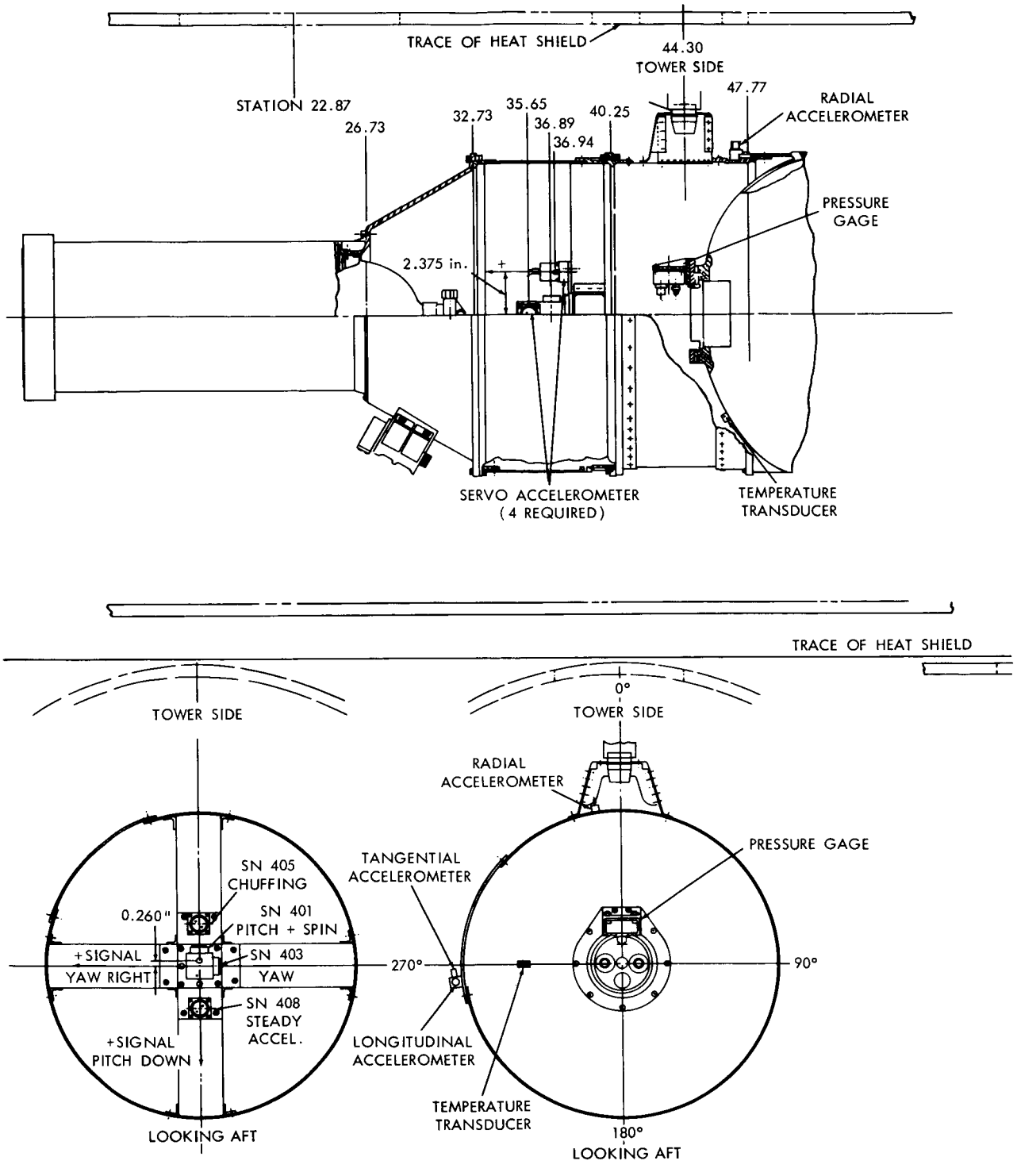

Figure 7–Transducer locations.

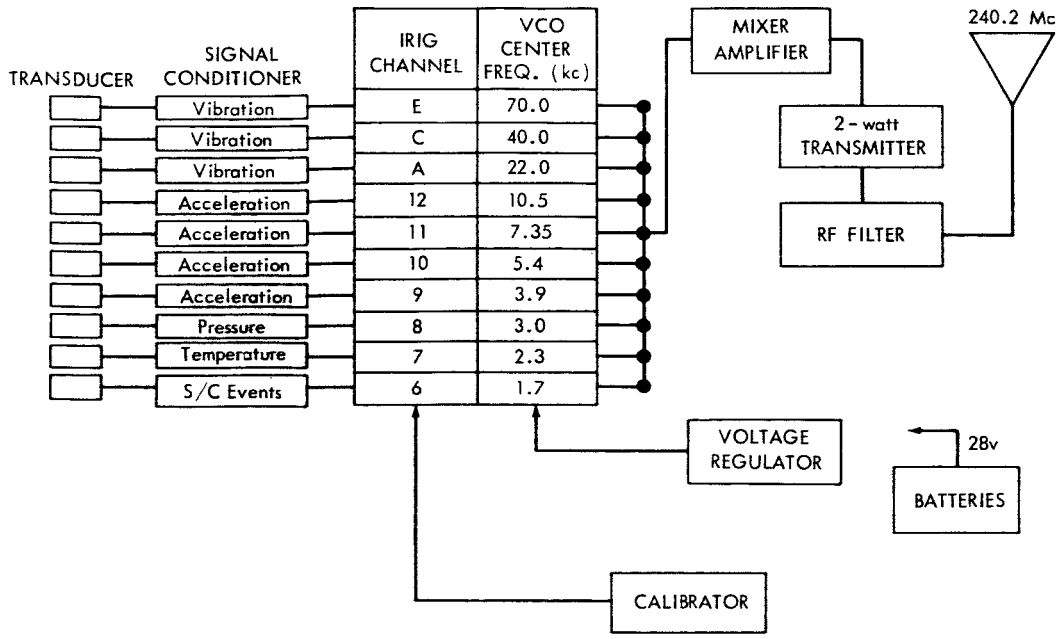

Figure 8—The experiment.

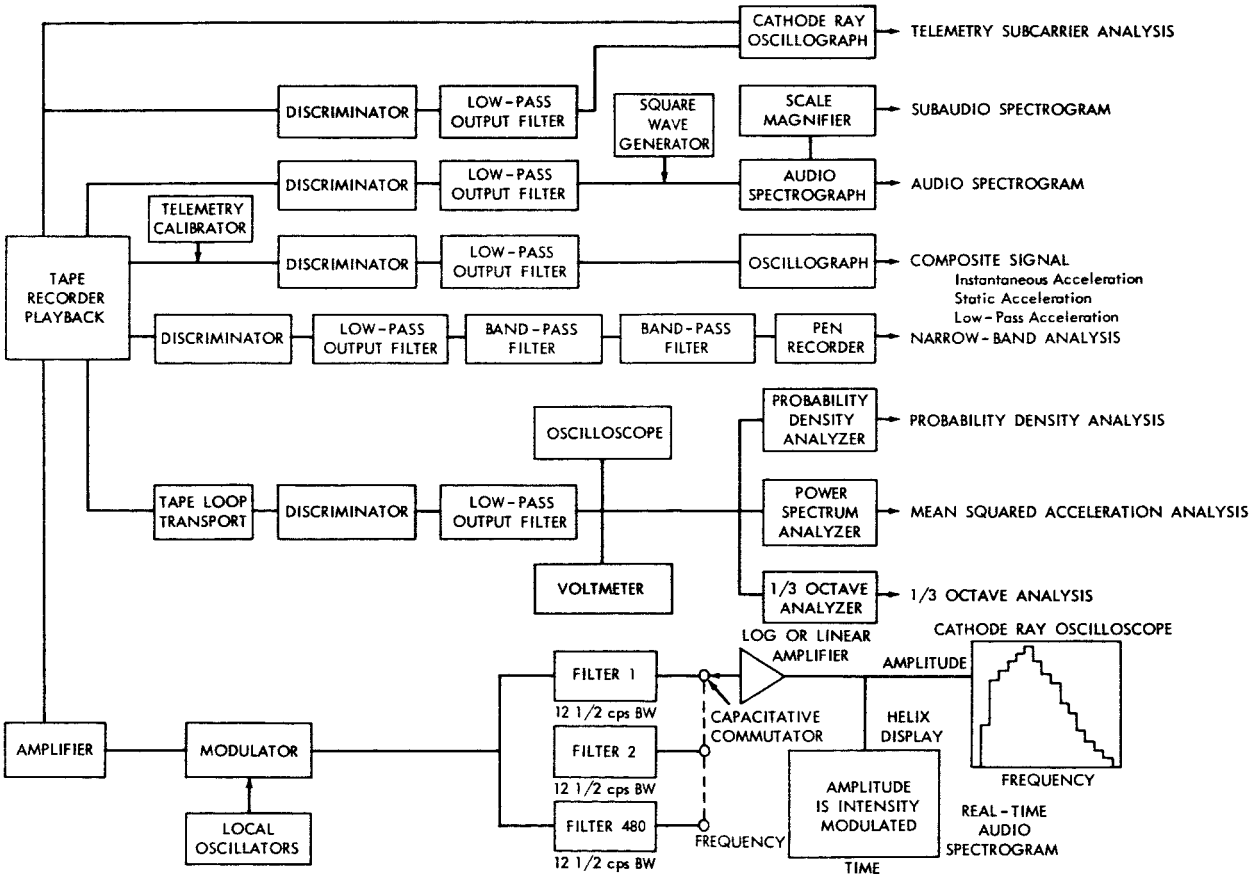

Figure 9—Data reduction system.

2. Evaluation of the telemetry subcarriers during the flight times of interest for relative amplitude and intermodulation noise level,

3. Detailed analysis to describe the frequency composition and relative amplitude of the vibration data,

4. Low-pass filtering for presentation of low-frequency data.

The users of these data, particularly when they are not intimately connected with the data gathering and analysis process, must be assured of the validity and effectiveness of the reduced data. Therefore this report follows, as much as possible, the recommendations of the American Standards Association, Inc. in its second draft of a "Proposed Standard Method for Analysis and Presentation of Shock and Vibration Data."

In particular, it is pointed out that:

1. These vibration data have not been corrected for the attenuation of high frequencies caused by the low-pass filters used in the experiment and the IRIG low-pass output filters used in the ground station discriminators. Figure 10 gives the end-to-end frequency response curves to be used in correcting the vibration data presentations.

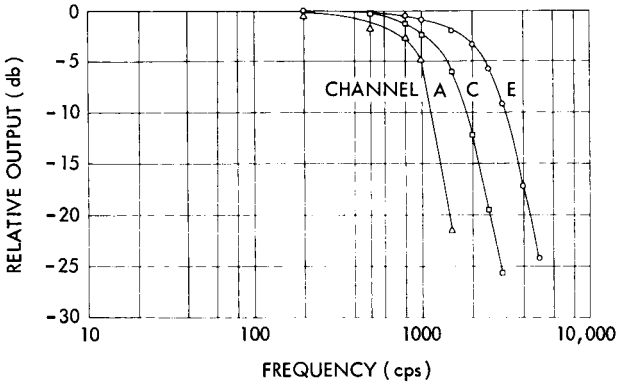

Figure 10—Frequency response of the vibration experiment and playback instrumentation.

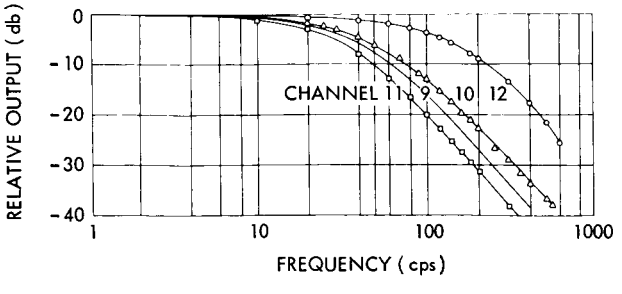

Figure 11—Frequency response curves for the low-frequency accelerometers.

2. The low-frequency servo accelerometers have a limited frequency response; therefore, high-frequency vibrations are not shown by these accelerometers. They are meant only to measure steady accelerations; however, their frequency responses are shown in Figure 11.

3. The time histories of temperature, pressure, and acceleration are corrected for the amplitude nonlinearities associated with the telemetering and data reduction systems.

4. The accelerometers (both types) were calibrated at GSFC, and the sensitivities are shown in Table 2. The vibration channels were calibrated end-to-end just prior to launch, and the calibrations recorded on magnetic tapes were used during the data reduction program.

5. The local structural responses where the vibration transducers were located could not be determined because of their proximity to the solid rocket motor.

FLIGHT TIME HISTORY

As a reference for the data and for information, the predicted time histories of axial acceleration, dynamic pressure, mach number, and altitude are presented in Figure 12. Table 3 lists the sequence of events and their predicted time of occurrence.

DISCUSSION AND RESULTS

Discussion

Although the primary purpose of the performance experiment was to obtain data relative to X-258 performance, vibration and acceleration data were also obtained during the first three stages of burning. The telemetry ground stations provided good coverage, and no data were lost. The down-range ship could not be at the optimum location with respect to the antenna pattern and flight trajectory because of other range commitments; therefore, with each revolution of the fourth stage, two signal nulls occurred as each of the two flight antennas revolved away from the receiving antenna. These nulls, seen in the fourth-stage real-time oscillograph record (Figure 38) precluded normal detailed analysis of the vibration data. Since the signal level between nulls is of the same order of magnitude as the background noise level, with the exception of perturbations at ignition and burnout, it was not considered necessary to attempt any further analysis. Similar low-level vibrations were obtained during a simulated high-altitude firing of an X-258.* Vibrations measured during first- , second- , and third-stage burning are presented in this report.

Detailed analysis of the vibration data was carried out only on channel E, since high frequencies are attenuated on channels C and A because of filter rolloff characteristics. The reader is reminded to keep the frequency response characteristics of each channel in mind when examining the data.

It is not the intent of this report to analyze vehicle performance, that is, flight trajectory, motor performance, vehicle motions of tipoff and coning, etc. These data have been made available to the vehicle contractor and to the Langley Research Center for analysis. The recorded data have been presented in this report for information only.

Random Vibrations

Random vibrations recorded during rocket flights usually are a consequence of airborne noise transmitted to structure as a result of reflected rocket flow from the pad and aerodynamic noise produced as the vehicle approaches mach 1 and maximum dynamic pressure. Resultant vibrations are dependent on the following external conditions: type of pad and pad deflector, acoustic "transparency" of the payload heat shield, heat shield profile, vehicle surface configuration,

*Tereniak, *op. cit.* (See Figure 34 for a real-time record of longitudinal vibrations shown in this report.)

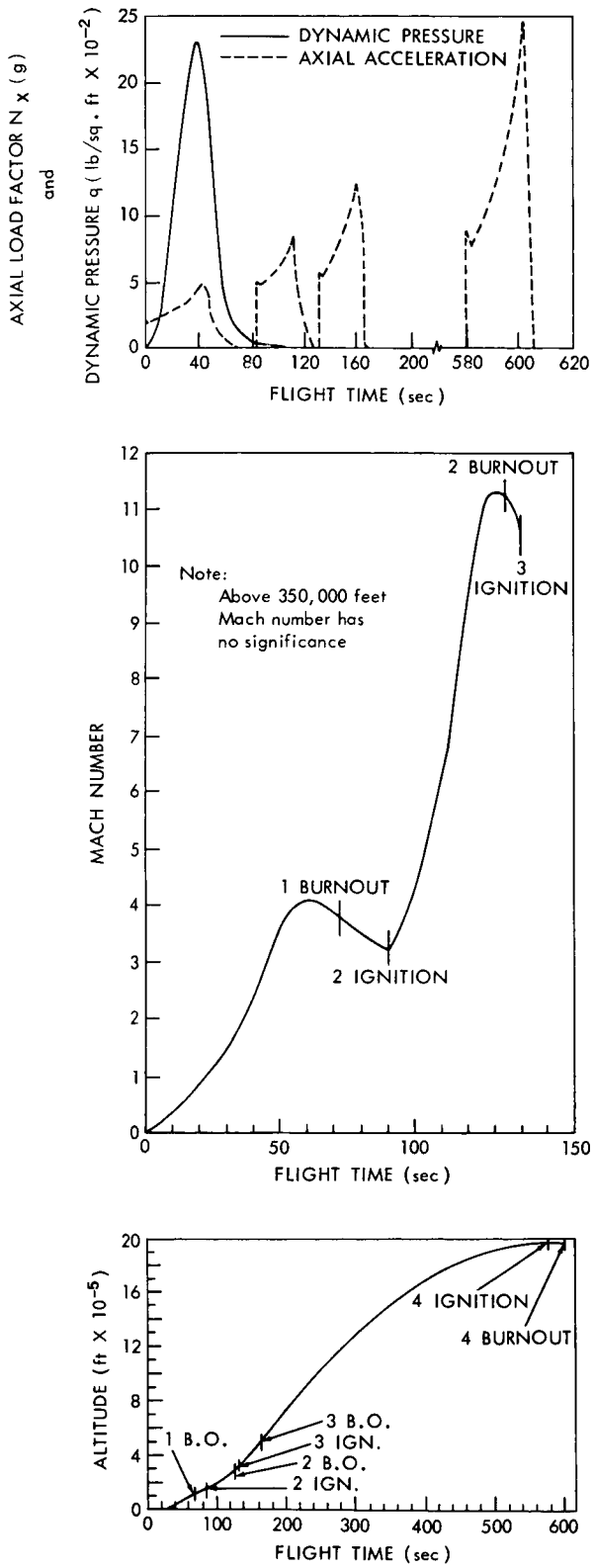

Figure 12–Nominal flight parameters for Scout S-122.

Table 3

Sequence of Events and Pitch Program

Time (sec)	Event
00.00	(1) Stage 1 ignition (2) $\dot{\theta}$ = 0.0000 deg/sec
00.20	Start timer
03.00	$\dot{\theta}_{c,1}$ = -3.57155 deg/sec
08.00	$\dot{\theta}_{c,2}$ = -0.72735 deg/sec
26.00	$\dot{\theta}_{c,3}$ = -0.53571 deg/sec
40.00	$\dot{\theta}_{c,4}$ = -0.32500 deg/sec
64.00	$\dot{\theta}_{c,5}$ = -0.36053 deg/sec
68.20	Stage 1 burnout
85.01	(1) Stage 2 ignition (2) Activate "B" controls (3) Separate first stage (4) Remove first-stage controls (5) Switch in body bending filter
102.00	$\dot{\theta}_{c,6}$ = - 0.18056 deg/sec
127.50	Stage 2 burnout
130.80	(1) Separate payload heat shield (2) Activate "C" burn controls (3) Third-stage squib ignition
132.50	(1) Stage 3 ignition (2) Separate second stage (3) Remove second-stage controls
138.00	$\dot{\theta}_{c,7}$ = -0.11956 deg/sec
165.90	Stage 3 burnout
170.90	(1) Activate "C" coast controls (2) Switch out body bending filter
187.00	$\dot{\theta}_{c,8}$ = - 1.00000 deg/sec
224.82	$\dot{\theta}_{c,9}$ = 0.00000 deg/sec
574.33	(1) Spin motor ignition (2) Fourth-stage squib ignition
575.83	(1) Explosive bolt ignition (2) Separate third stage
576.83	Retro-force command
580.33	Stage 4 ignition
606.33	Stage 4 burnout

vehicle trajectory, and atmospheric conditions. Reference 1 shows that higher vibration levels during transonic and maximum dynamic pressure (max. q) can be expected with a bulbous-type heat shield rather than a "clean" cone-cylinder heat shield.

As a reference for the random vibrations recorded during first-stage burning, Figure 12 gives a time history of altitude, mach number, and dynamic pressure and Figure 13 shows the wind conditions at launch. Figure 1 indicates the slightly bulbous profile of the heat shield, in addition to the "dry" launch pad.

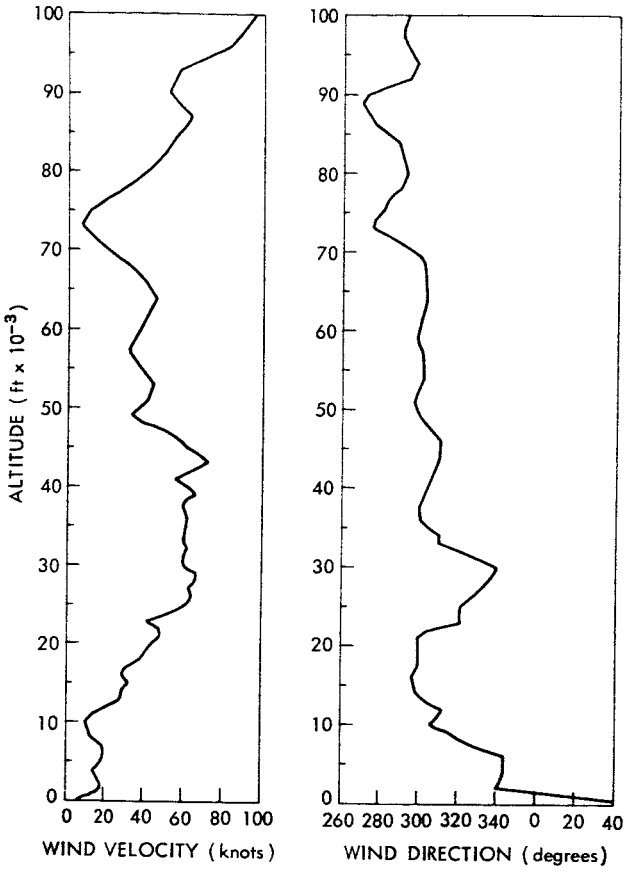

Figure 13–The wind conditions at launch of Scout S-122.

Figure 14,* a real-time oscillograph record for first-stage burning, presents the random vibrations recorded by the high-frequency accelerometers during the periods of liftoff, mach 1, and max. q. The peaks for channel E at these times average ±1.5g and do not exceed ±3g. Figure 15, a g-rms vibration time history of the three vibration channels, shows no levels above 1 g-rms. The frequency content and relative magnitude of the vibrations for the three channels during the first-stage burn period are given in Figures 16, 17, and 18, which are real-time "quick look" spectrum analyses. The display is a frequency (20 cps to 5 kc) versus time characteristic and is linear with respect to both parameters. The relative vibratory level is indicated by the shading between gray and black – the black indicating the higher level. The spectrograph display is the output of 480 magneto-restrictive filters, each having a bandwidth of 12.5 cps. The spectrum appears to be broad above 700 cps; this was confirmed by a 1/3 octave analysis (not included in this report) and by a detailed analysis of magnetic tape loops, performed on a wave analyzer.

The detailed spectrum for mach 1 is presented in Figure 19 (note that the transient at T+18.31 has been cut out of the loop). The acceleration density is low (below 0.0016 g^2/cps), and the spectrum is broad with no strong peaks. Figure 20 shows the power spectrum for the max. q and its corresponding probability density curve. A check of the stationarity of the data recorded during the max. q portion of flight was performed by cutting the 8-second data loop into two 4-second loops. Power spectral density (PSD) and probability density (PDA) plots were run on each loop, as presented in Figure 20. An assumption of stationarity is supported by the similarity of all three PSD and PDA plots.

*Figures 14 through 38 follow the text in this report (pages 17 through 48).

From T+3 to T+7, a buildup in random vibrations was recorded on channel E; however, the buildups on channels C and A at this time are not valid data (see Figure 14). Analysis of the subcarriers showed a definite breakup of channels C and A – indicating noise, not data. Channel E subcarrier was normal. The detailed power spectrum analysis given in Figure 19 is similar to the spectra at mach 1 and max. q in level, but the frequency spectrum is broader. Reference 2 indicates that, from past static firing data, a buildup in thrust usually occurs between 5 and 15 seconds. The chamber pressure curve in Reference 2 shows a rapid increase from approximately T+8 to T+10. Reference 2 further states that "from all indications an ignition characteristic of the propellant surface affects both the burning surface and burning rate." Examination of high-speed motion picture color film of the launch shows a brown plume at T+2.7 which suggests a burning irregularity.

At T+19.79, an abrupt increase in vibration level was recorded on all three channels, probably the result of some burning irregularity of the rocket motor. Examination of high-speed motion picture color film of the flight shows the rocket plume becoming brilliant at this time. An enlargement of the motion picture frame showing the brilliant plume is presented in Figure 21. A power spectrum analysis was performed and is shown in Figure 19. The spectrum shape is similar to that at mach 1 and max. q; however, the level is higher, as expected. The increase in the high-frequency range cannot be explained with the limited amount of data available. The subcarriers were extensively analyzed, and the data are valid. A high-speed real-time oscillograph record (Figure 22) shows the abrupt change in level. Vibration levels on channel E increase by a factor of 2 (see Figure 15).

Transient Vibrations

Transient vibrations were recorded at stage ignition, during first-stage burn because of some motor burning irregularity, and during third-stage burning when the igniter deflector passed through the motor nozzle.

The liftoff transient recorded on channel E is presented in Figure 23. The transient reached a maximum amplitude of $^{+8.4}_{-9.8}$g and damped out after approximately 8 cycles. The 1/3 octave band analysis showed this transient in the 50-cps band.

The transient recorded on channel E during first-stage burn at T+18.31 was, likewise, in the 50-cps 1/3 octave band and is given in Figure 22, a real-time oscillograph record. The transient reached a maximum amplitude of approximately ±2g at the second cycle and damped out after 8 cycles. Reference 2 states that "... such disturbances might be caused by graphite material emanating from the area immediately downstream of the throat." The contractor further states that a similar disturbance occurred during a static firing and during another flight. Figure 21 shows a sequence of high-speed motion picture color films taken at this time. The film shows the brilliant plume flare followed by black smoke and unidentified pieces of material emanating from the plume. Figure 21 also shows pieces coming out of the plume during the time period of T+27 to T+29. The vibration records do not indicate any effect at this time.

At third-stage ignition, approximately ±7g was recorded by channel 12, the low-frequency longitudinal accelerometer, for the first cycle. The 70-cps signal exponentially decayed and damped out after approximately 10 cycles (see Figure 24).

The third-stage igniter deflector passing through the rocket nozzle* caused an exponentially decaying sinusoid whose maximum amplitude was approximately ±10g. Its frequency was 90 cps, and it damped out after 22 cycles. Figure 25 gives this transient recorded on channel E and channel 12, the low-frequency longitudinal accelerometer. Both accelerometers recorded ±10g maximum amplitude.

The amplitudes of all the previously mentioned transients do not include the positive value of steady axial acceleration.

Low-Frequency Oscillations

Low-frequency oscillations were observed on this flight during the first three stages of burning (see Figures 14, 26, and 27, respectively first- , second- , and third-stage real-time oscillograph records). The frequencies shown most predominant by analysis with a subaudio spectrograph are plotted in Figure 28. An analysis performed on the low-frequency pitch accelerometer, channel 10, illustrates vehicle pitching and lateral bending frequencies. The composite signal of the low-frequency pitch accelerometer was passed through a narrow-band filter to show the most predominant frequencies and their amplitudes (see Figures 29, 30, and 31).

At first-stage ignition, the vehicle's first lateral bending frequency of 3.2 cps was excited as shown in Figure 14. After reaching an amplitude of ±1/2g at the first cycle, the signal exponentially decayed and damped out at approximately T+9 and became more pronounced at T+35, persisting to T+62 with a slight increase in frequency (see Figures 28 and 29). Low-level sinusoids near 60 cps came in and out from T+46.5 to T+58.

During second-stage burn, 7.5 and 17 cps were most predominant on the spectrogram. A harmonic at 16 cps also was evident. The real-time oscillograph record (Figure 26) indicates that the amplitude varies between +0.75 and +0.95g for the first 18 seconds and then diminishes to lower amplitudes, with the wave shape consisting principally of the fundamental frequency (see Figures 27, 30, and 31). The low frequencies are also evident on channels C and A in Figure 26.

At third-stage ignition, the pitch accelerometer experienced a peak amplitude of ±1g, then exponentially decayed to approximately ±0.1g in 2.4 seconds (Figure 27). The predominant frequency was 15.5 cps at ignition, sliding up to 20.7 cps at burnout. The vibrations remained at a low level with the exception of a slight buildup 20 seconds after ignition (Figure 31).

*Private communication with S. Salmirs, NASA Langley Research Center.

Acceleration, Pressure, Temperature, and Spin Rate

Axial acceleration, recorded on channel 12, is plotted in Figures 32 and 33. First- and third-stage acceleration time histories were nominal, while second-stage acceleration was slightly low and the burntime was long. Fourth-stage maximum acceleration was higher than normal, and the burntime was shorter than expected for a spinning motor; however, the tail-off was exceedingly long. The ±1/2g longitudinal accelerometer showed no evidence of X-258 chuffing.

An X-258 headcap pressure time history is shown in Figure 34, and a real-time oscillograph record of pressure in Figure 35. Note in Figure 35 that the pressure gage reads sea-level pressure inside the motor before ignition and pressure at altitude after burnout. A nozzle diaphragm is blown out with ignition.

A time history of X-258 motor dome temperature is presented in Figure 36. The dome temperature reached 620°F when the telemetry signal was lost by the down-range ship, 465 seconds after fourth-stage ignition. The curve is interpolated from loss of signal to telemetry acquisition by the South African station. Maximum dome temperature measured on an X-258 launched from Wallops Island, Virginia,* on April 15, 1964, is shown on this plot to illustrate the possible correlation between the two measurements and to aid in the interpolation. Although the temperature transducers were located at similar points, there were some differences that may invalidate correlation of the two maximum points. The dome of the Wallops-launched X-258 was covered with aluminum paint whereas the S-122 X-258 dome was covered with layers of aluminum foil, fiber glass, and aluminum foil as shown in Figure 5. The final temperature point on the plot, 423°F, 2 hours after X-258 ignition, was recorded at South Point, Hawaii, on the first pass.

A plot of spin rate versus time, Figure 37, was obtained from the low-frequency pitch accelerometer located 0.260 inch off payload centerline and, as was previously mentioned, from the frequency of the RF signal dropouts as the antennas rotated.

At ignition of the spin motors, the pitch, yaw, and longitudinal ±1/2g accelerometers exhibited low-frequency oscillations, as presented in Figure 35. Separation occurred 1-1/2 seconds later, imparting an axial acceleration to the payload for 55 milliseconds. The spin rate at this time was 159 rpm. With separation, the low-frequency oscillations subsided and a sinusoidal output began, indicative of coning. The X-258 ignited 4.705 seconds after separation, and the spin rate began to increase until it reached 169.5 rpm according to the frequency of the signal dropouts. This is in good agreement with the pitch accelerometer which indicated 170 rpm after burnout. The pitch accelerometer could not be used to determine spin rate during the burning phase because of the cross-axis acceleration component evident in Figure 35 for channels 9 and 10. This was caused by cross-axis sensitivity of the accelerometers (0.003g/g maximum) and some degree of thrust misalignment. The sinusoidal output is again evident after burnout but with a larger amplitude, indicating a larger coning amplitude.

*Ott, R. H., Jr., "Data Reduction and Analysis Results of Argo D-4, NASA 12.03 GT-G1 Test of X-258-C1 Rocket Motor," Goddard Space Flight Center Memorandum to J. F. Corrigan, May 26, 1964.

An analysis of the low-frequency accelerometer data has been performed by the flight vehicle contractor (Reference 2). The contractor reports that "Subsequent to fourth-stage burnout ... a coning amplitude of 5.6 degrees was calculated from the accelerometer data" and "... just prior to fourth-stage ignition ... The fourth stage was coning at a steady-state half-cone angle amplitude of 1.1 degrees."

Analysis of the telemetry tapes from South Point, Hawaii, indicates that the spin rate was near zero approximately 2 hours after spinup. Channel 6 indicated that all spacecraft events had occurred for successful spacecraft separation.

CONCLUDING REMARKS

The flight data presented in this report indicated:

1. Vibrations at the X-258 forward motor shoulder were practically nonexistent during the X-258 burning phase,
2. X-258 flight vibration levels are similar to those measured during a static firing at simulated high altitude (Figure 38),
3. Major vibration levels occurred during first-stage flight times of mach 1 and max. q,
4. First-stage motor burning irregularities caused increases in the random vibration level,
5. Vibration test specifications for X-258 Scout-launched payloads need to be revised.

Goddard Space Flight Center is cooperating with Langley Research Center in another performance experiment to be launched by an X-258 Scout in 1964. These additional data will be used to verify the results from S-122.

REFERENCES AND BIBLIOGRAPHY

References

1. Tereniak, W. B., and Clevenson, S. A., "Flight Shock and Vibration Data of the Echo A-12 Application Vertical Tests (AVT-1 and AVT-2)," NASA Technical Note D-1908, October 1963.
2. Ries, W. A., Jr., "NASA Scout S-122 Final Flight Report", Ling-Temco-Vought, Inc., Dallas, Report 3-30,000/4R-40, February 12, 1964.

Bibliography

American Standards Association, Inc., "Proposed Standard Method for Analysis and Presentation of Shock and Vibration Data," New York, N.Y., August 1962 (unpublished).

Eldred, K., Roberts, W., and White, R., "Structural Vibrations in Space Vehicles," Northrop Corp., Hawthorne, California, WADD TR 61-62; AD-273 334, December 1961.

Morrow, C. T., "Shock and Vibration Engineering," Vol. 1, New York: John Wiley and Sons, 1963.

Nagy, J. A., "Flight Vibration Data from the Thor Agena Vehicle used to Launch Alouette (1962$\beta\alpha$1)," NASA Technical Memorandum X-1003, December 1964 (Confidential).

Piersol, A. G., "The Measurement and Interpretation of Ordinary Power Spectra for Vibration Problems," NASA CR-90, September 1964.

Randall, F. W., Jr., and Green, M., "The Scout; Solid Propellant Launch Vehicle," Ling-Temco-Vought, Inc., Dallas, Revised October 1962.

Sinclair, C. W., "Scout S-122 Pre-Flight Planning Report," Ling-Temco-Vought, Inc., Dallas, Report 3-30,000/3R-316, November 27, 1963.

Williams, L. A., "Flight Vibration Data from the Delta 9 Launch Vehicle," NASA Technical Note D-1683, October 1963.

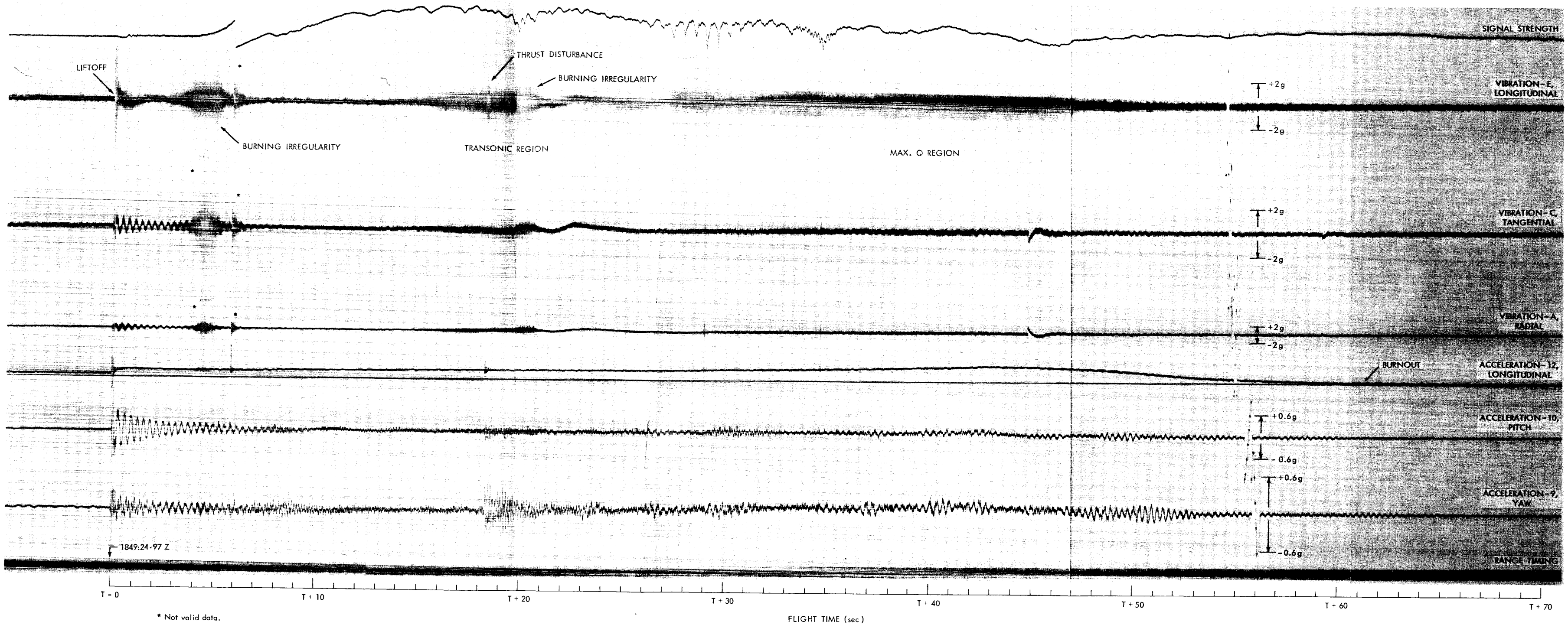

Figure 14—First-stage real-time oscillograph record.

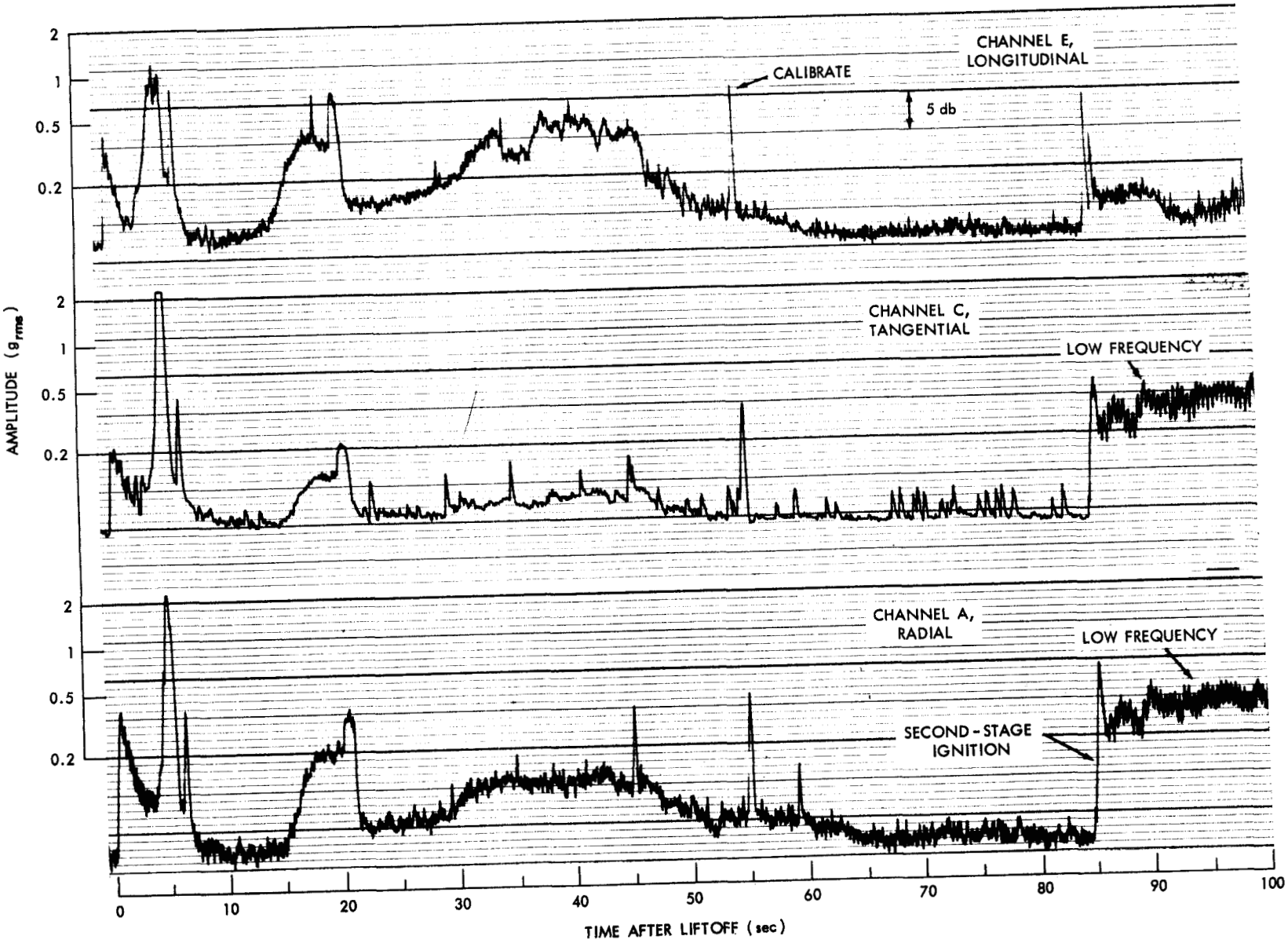

Figure 15–Rms-level vibration time history.

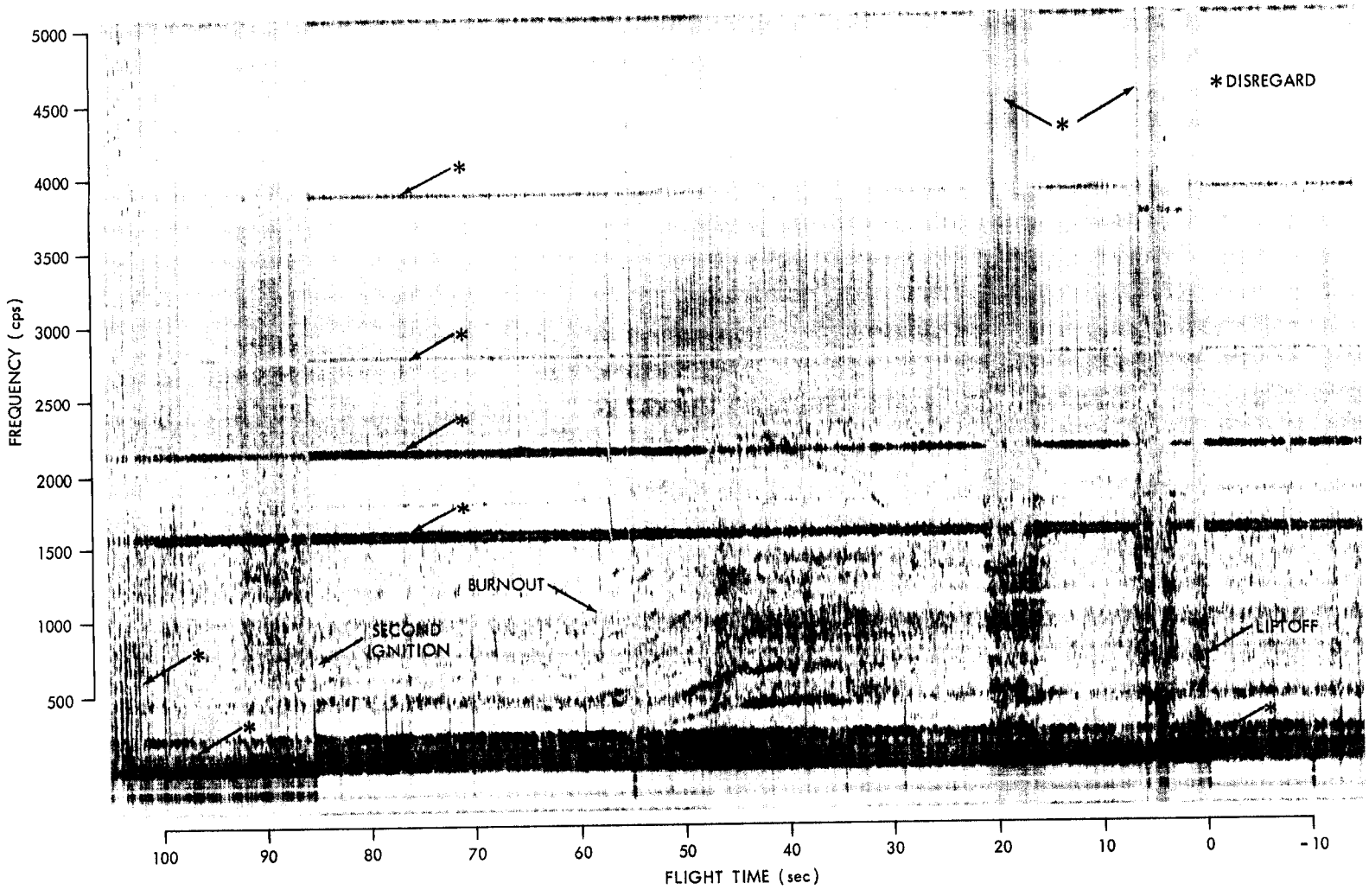

Figure 17–Real-time spectrograph of frequency vs. time vs. amplitude for accelerometer C.

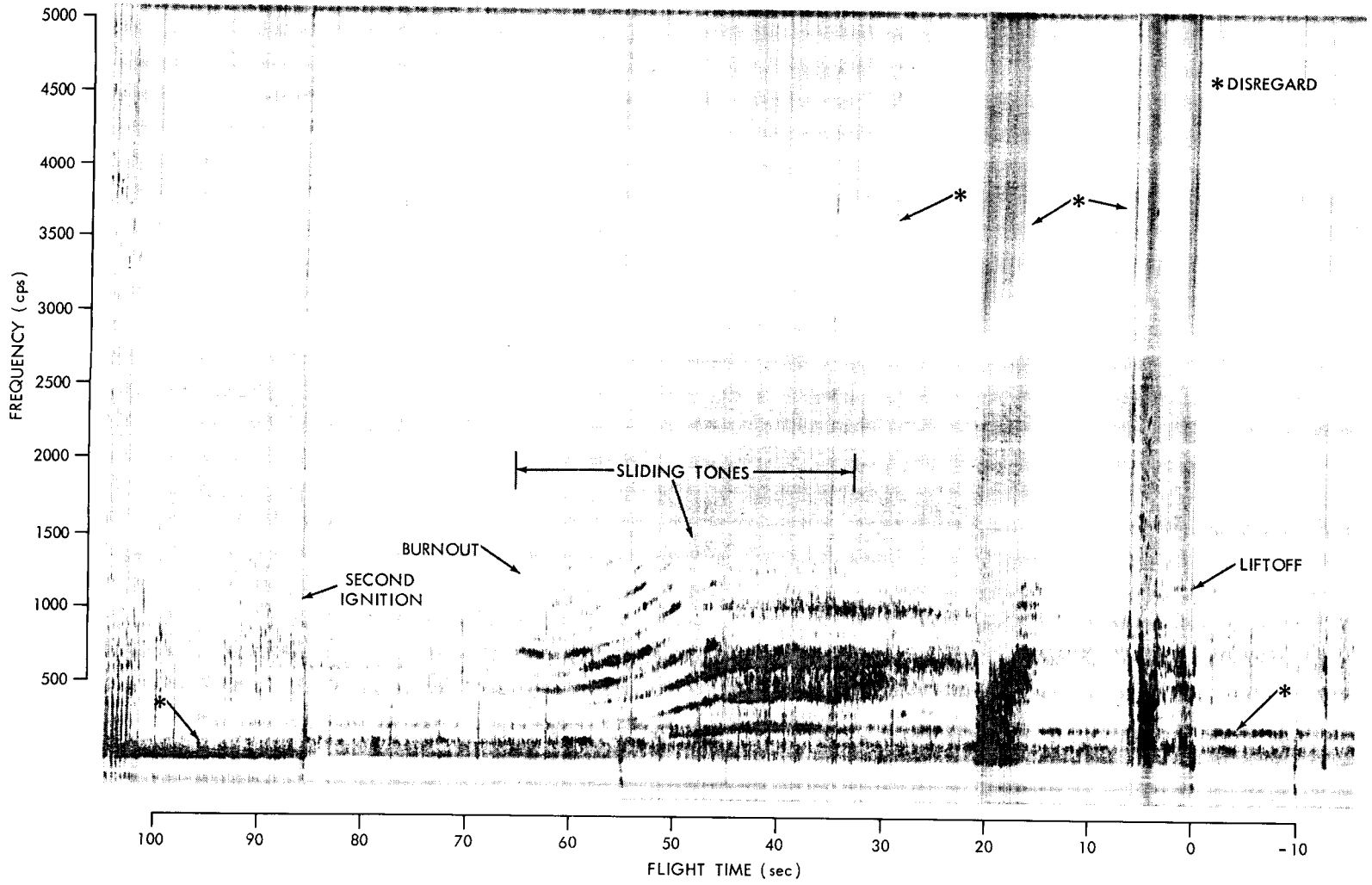

Figure 18–Real-time spectrograph of frequency vs. time vs. amplitude for accelerometer A.

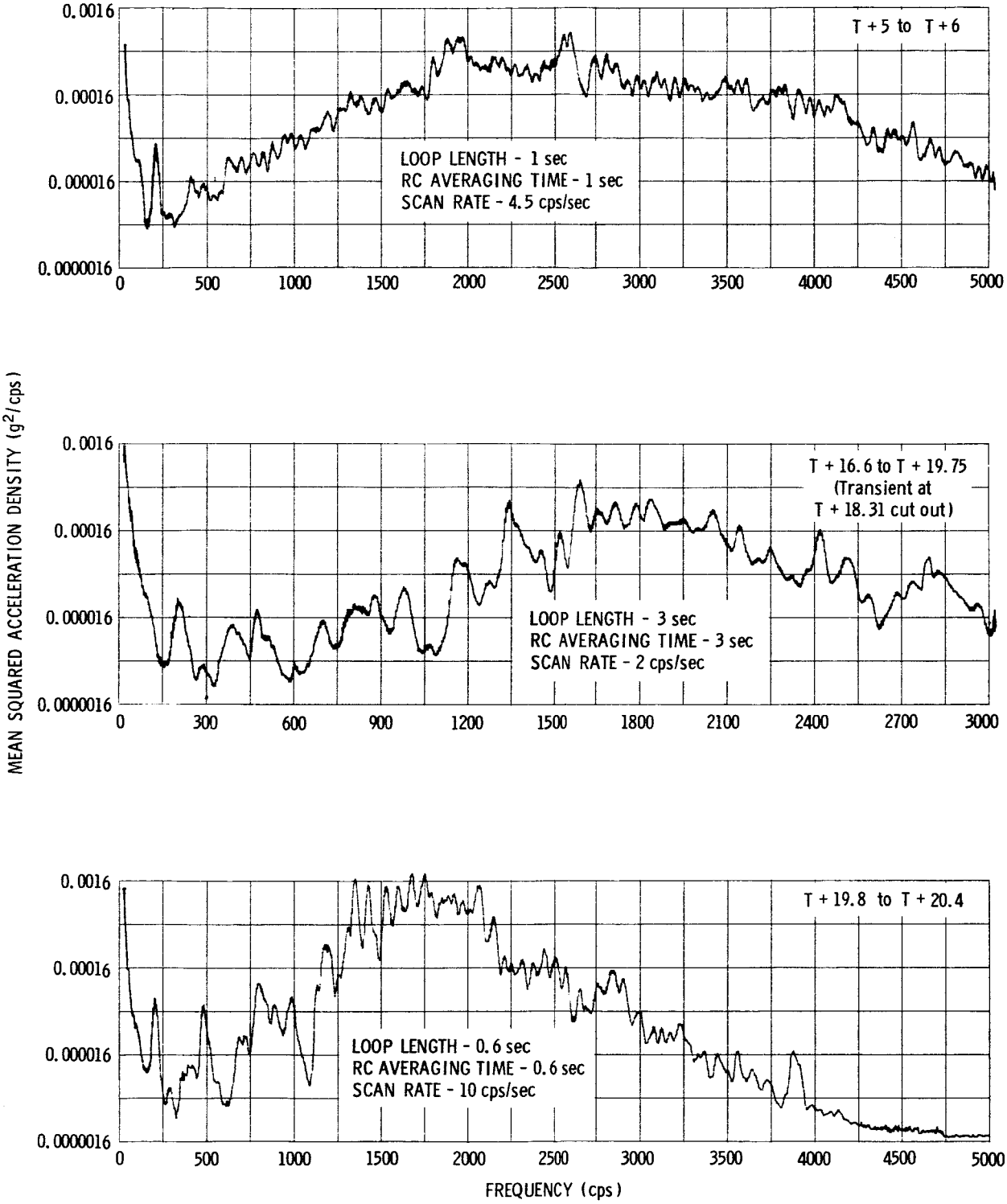

Figure 19—Channel E detailed spectral analysis. Effective filter bandwidth, 25 cps.

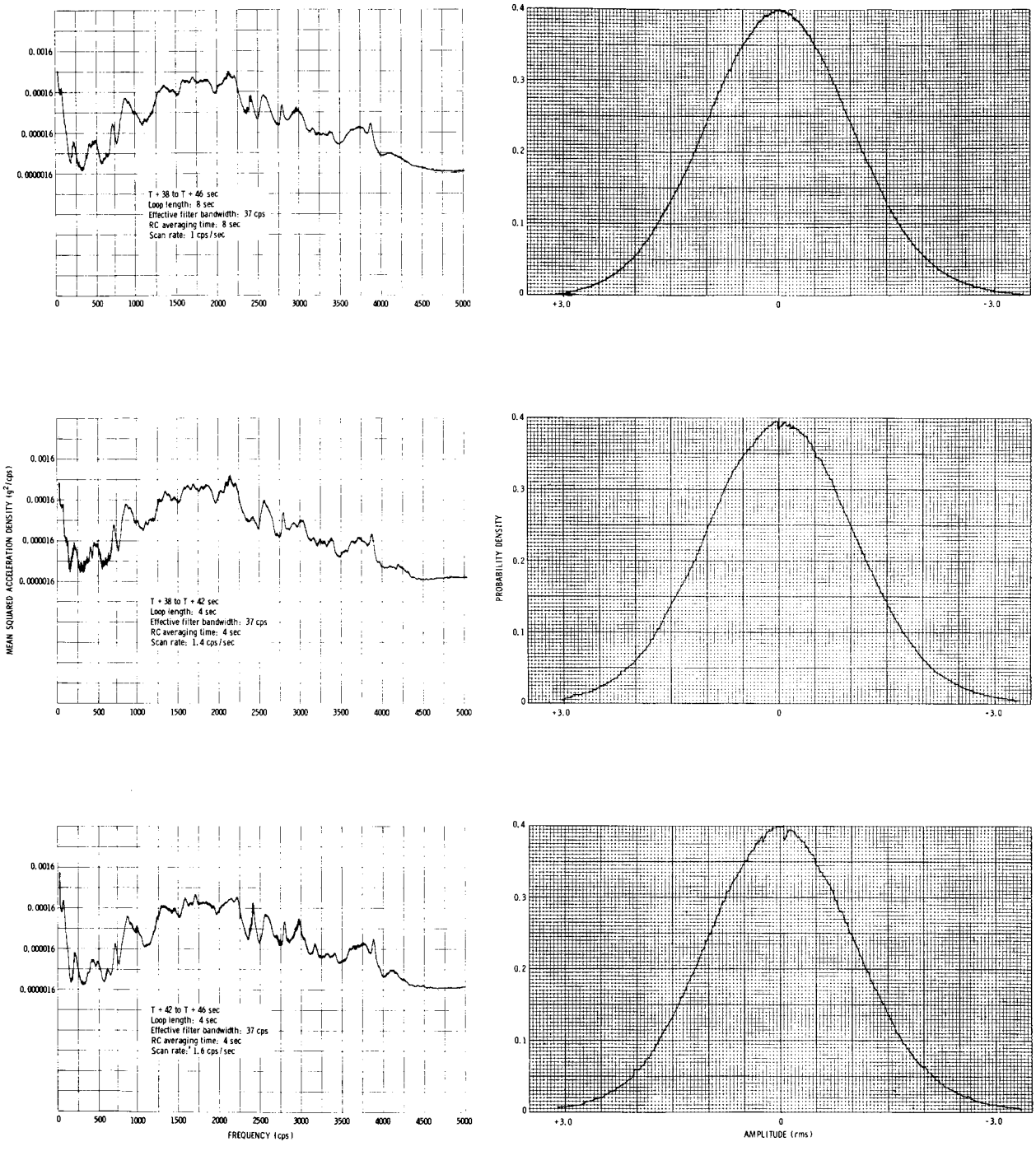

Figure 20–Channel E spectral analysis and probability density analysis for the maximum dynamic pressure phase.

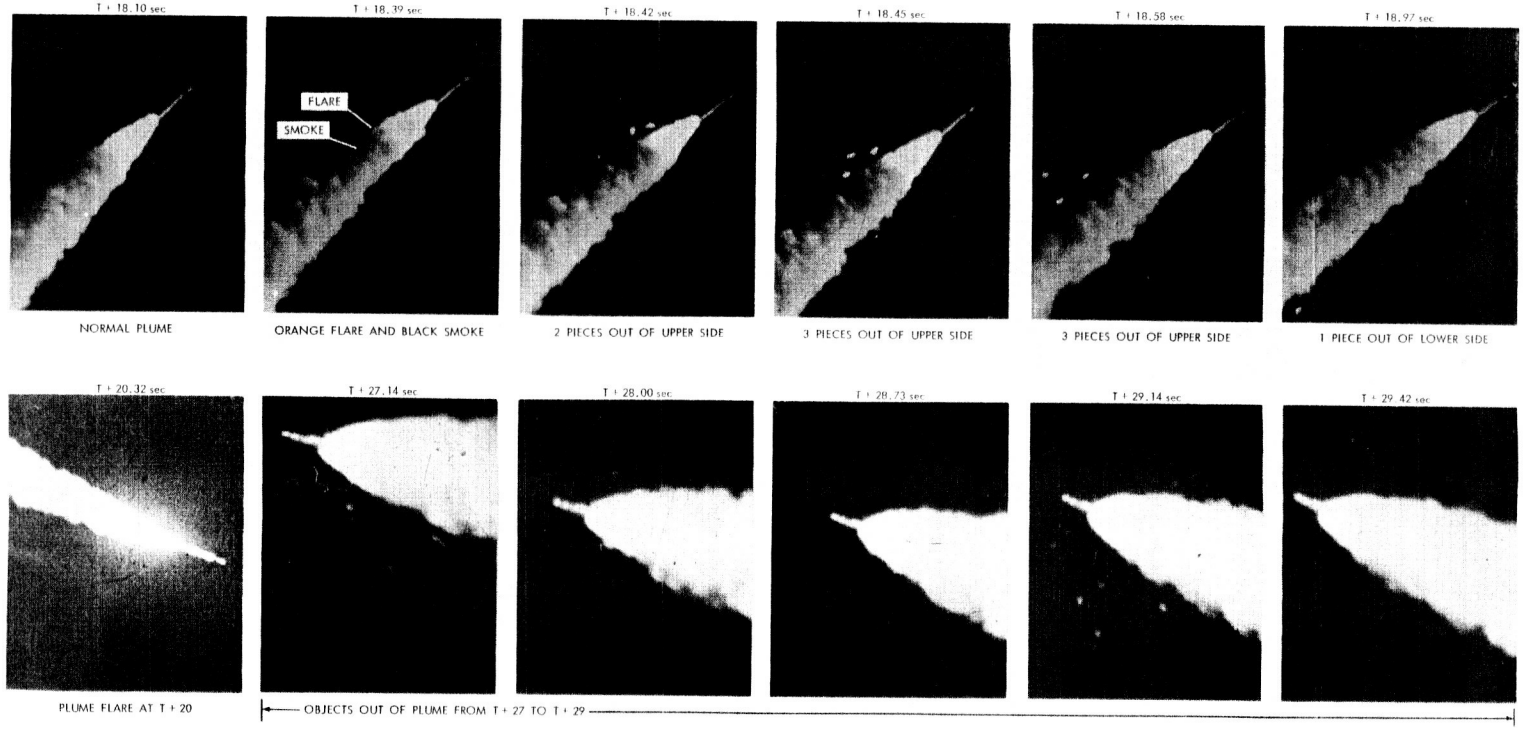

Figure 21–Motion picture frames of first-stage burning. (Upper set of pictures have been retouched.)

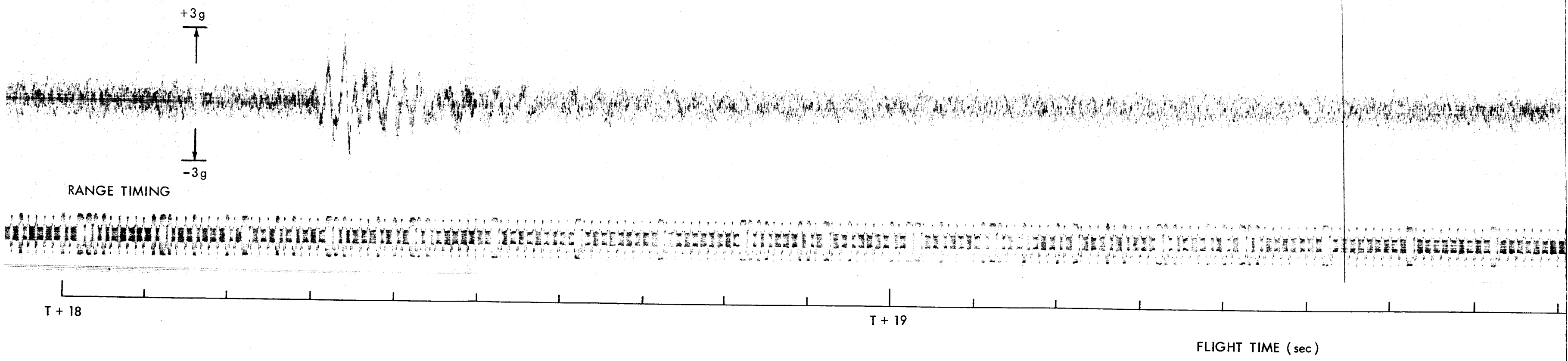
+3g
-3g
RANGE TIMING
T + 18
T + 19
FLIGHT TIME (sec)

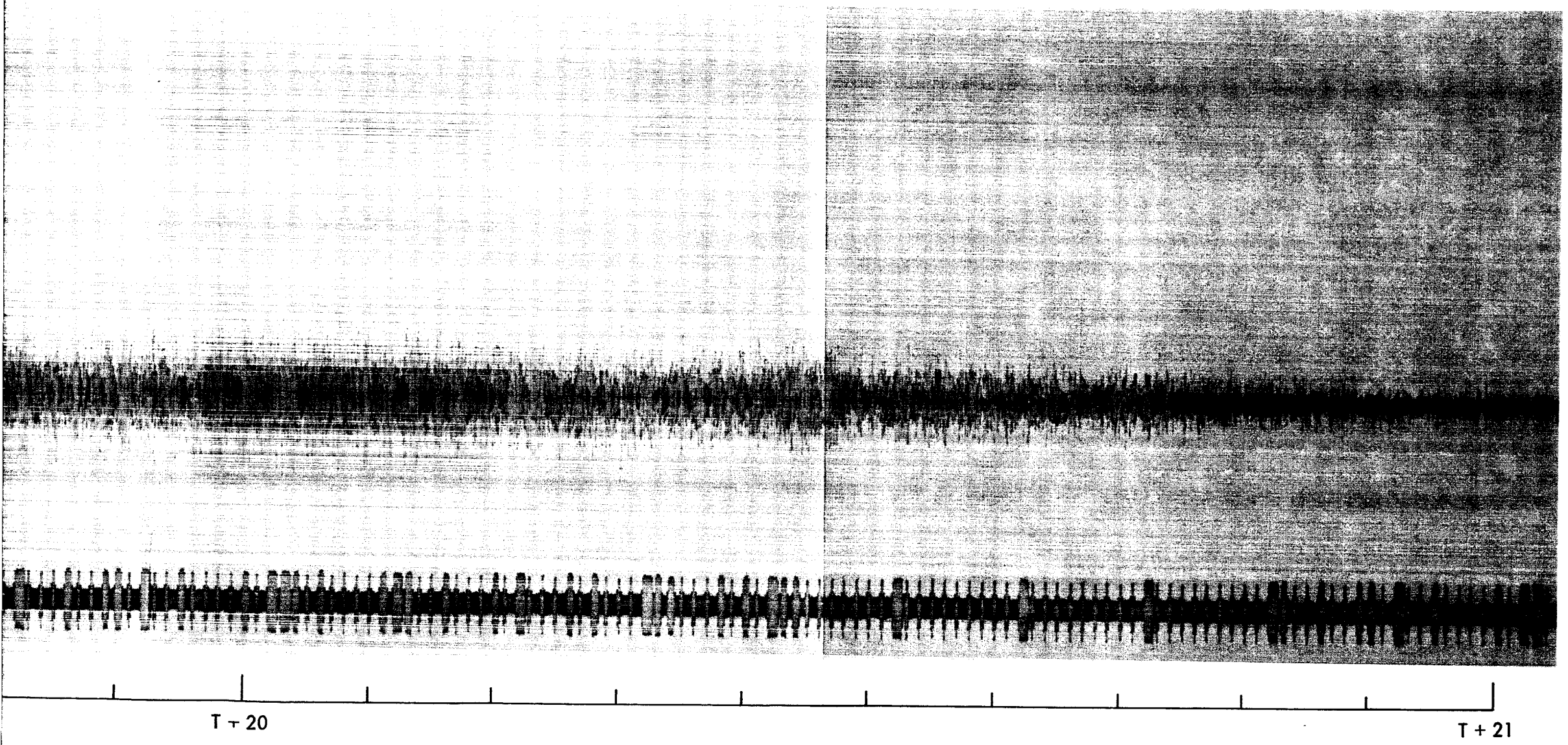

Figure 22–First-stage real-time oscillograph record showing thrust axis perturbations, channel E.

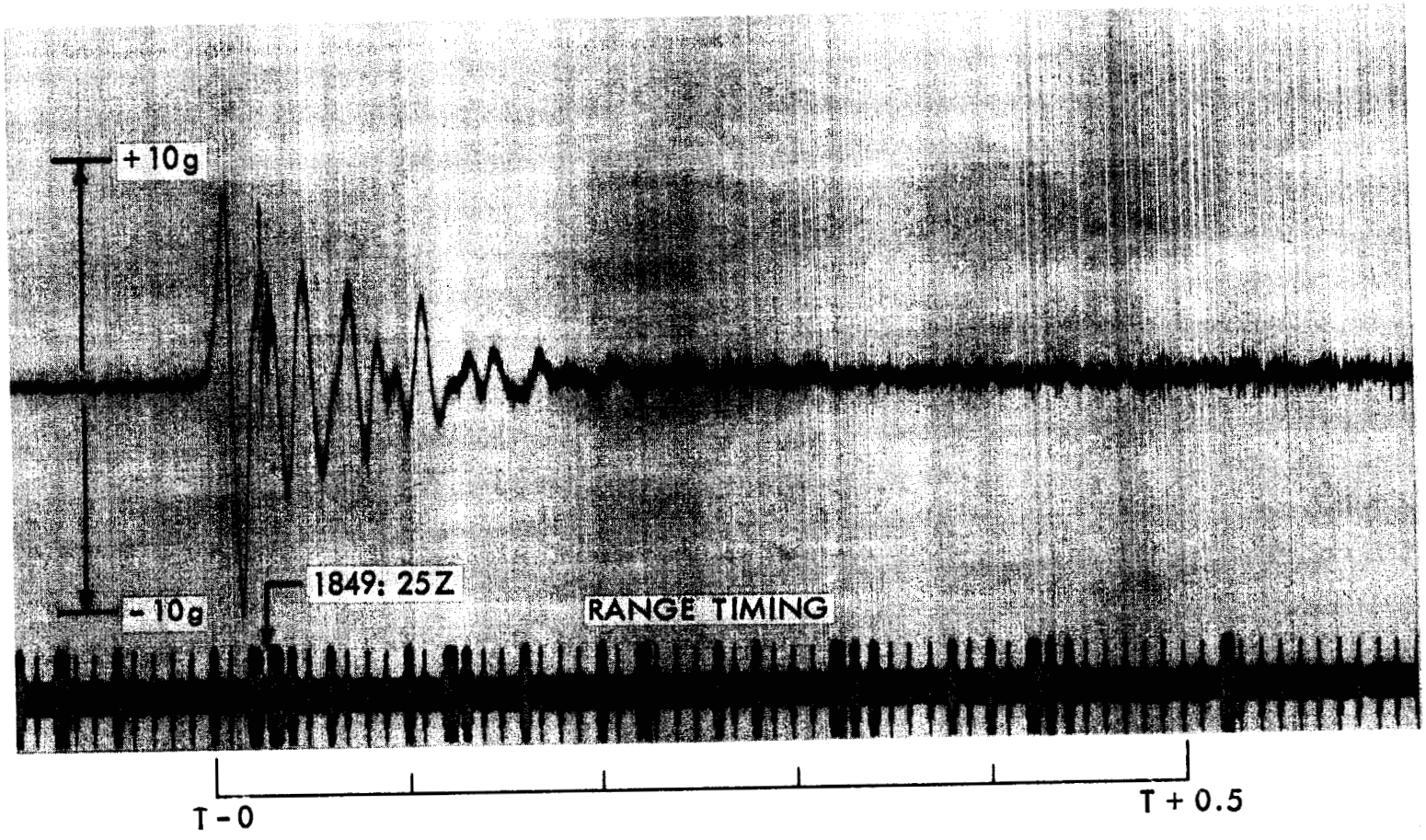

Figure 23–Liftoff transient, channel E.

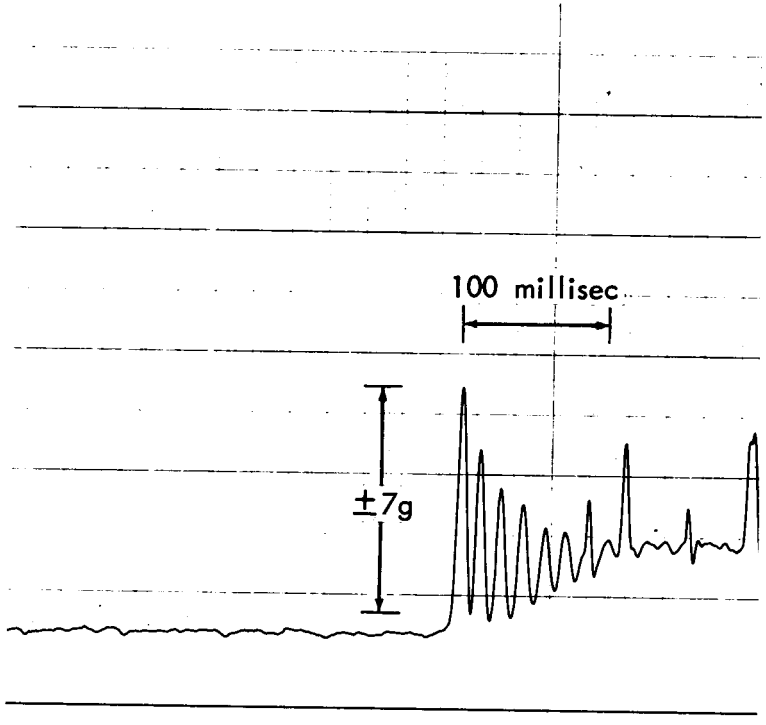

Figure 24—Third-stage ignition transient, low-frequency longitudinal accelerometer.

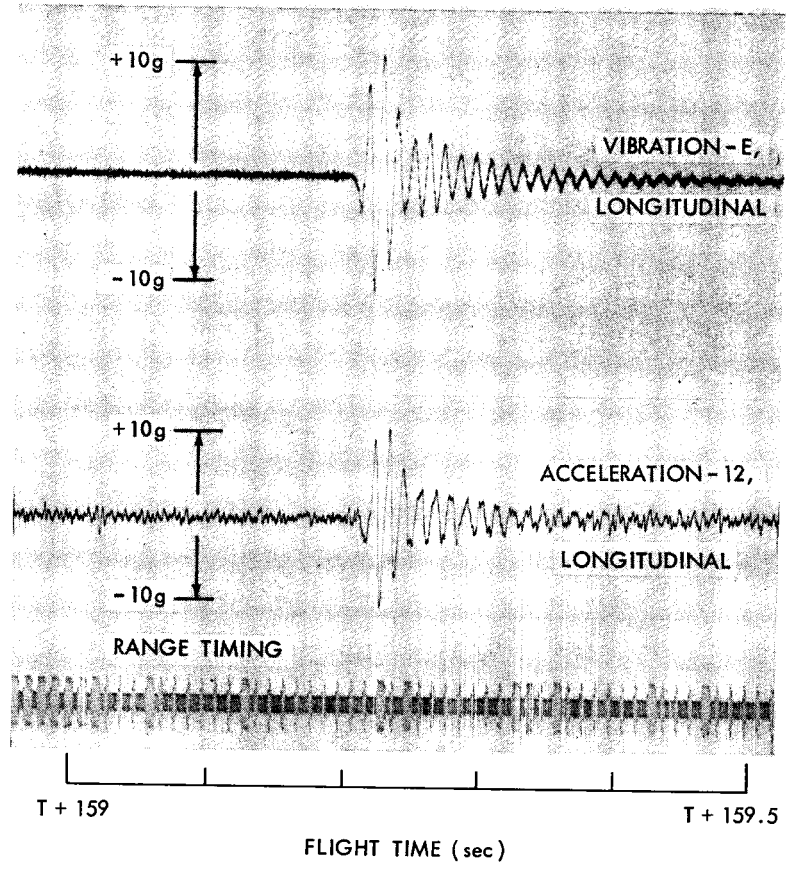

Figure 25—Third-stage thrust axis perturbation.

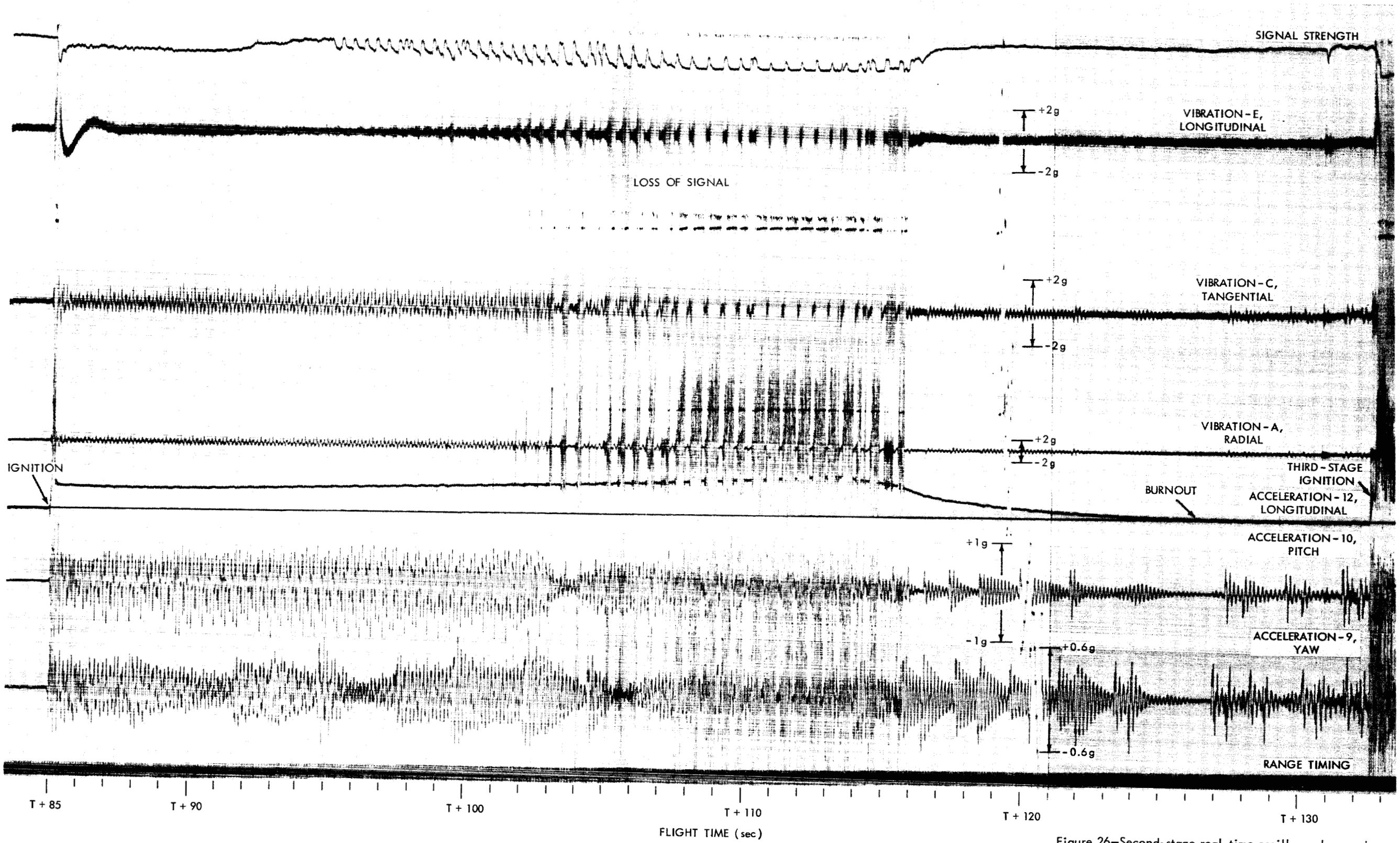

Figure 26–Second-stage real-time oscillograph record.

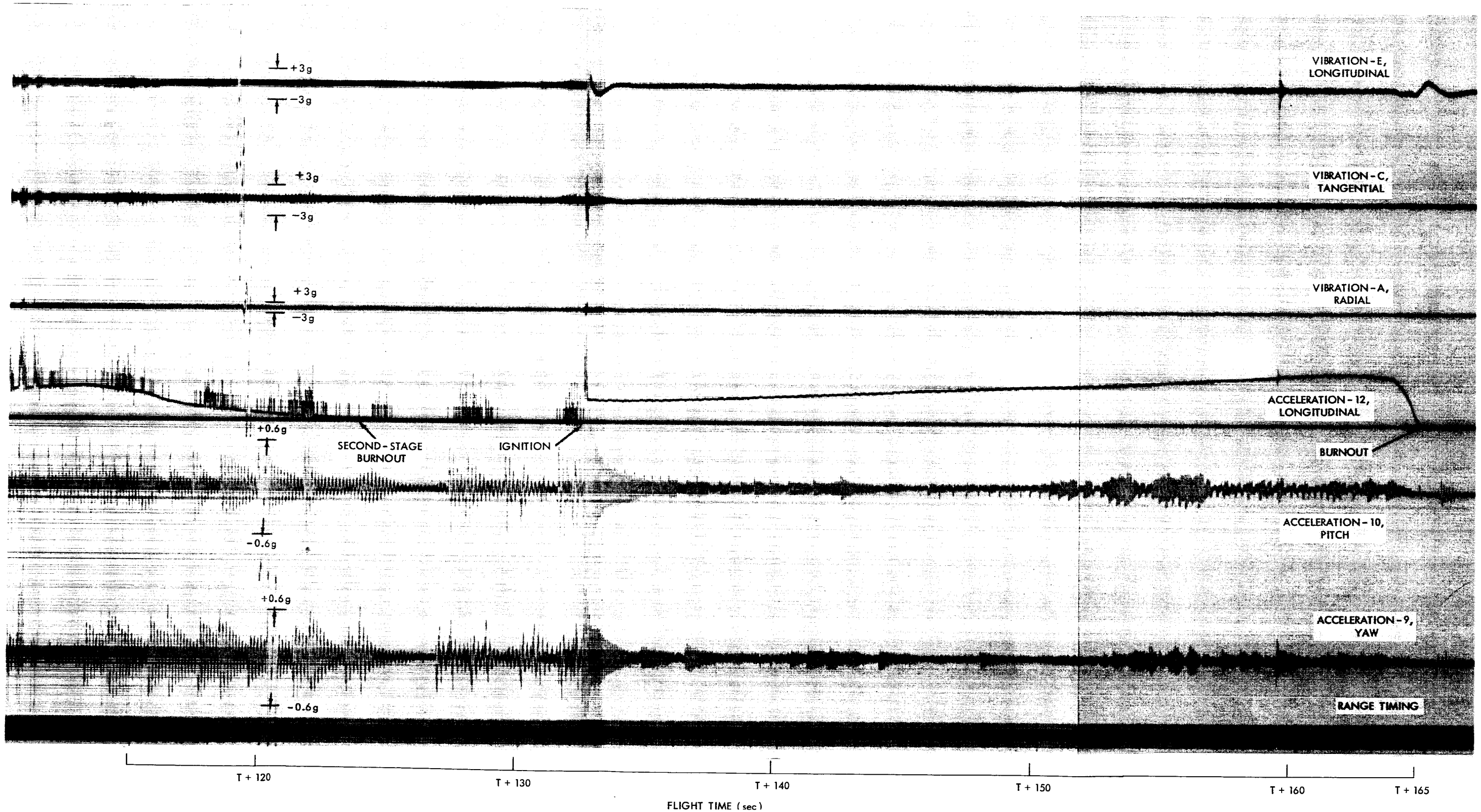

Figure 27—Third-stage real-time oscillograph record.

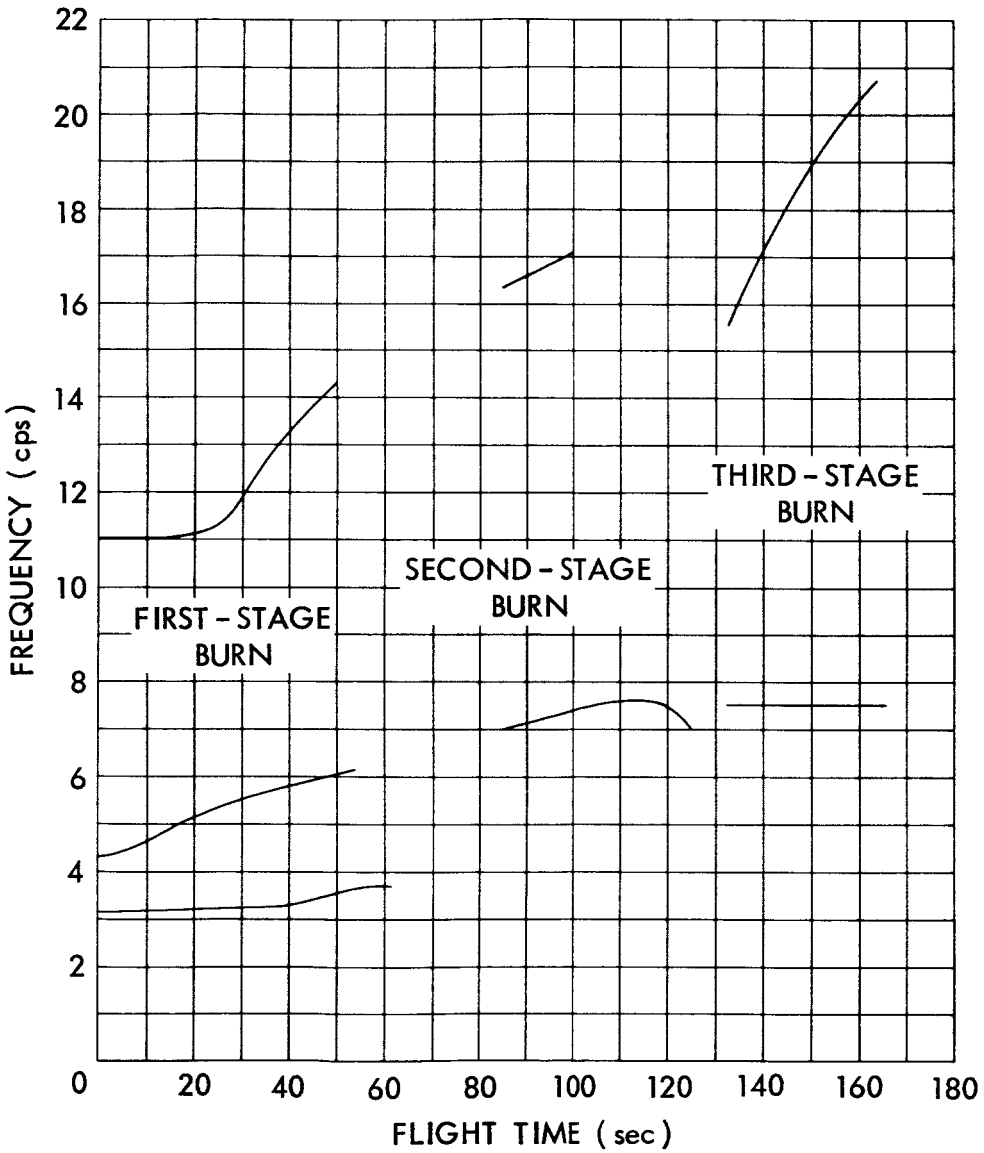

Figure 28–Vehicle pitching and lateral bending frequencies.

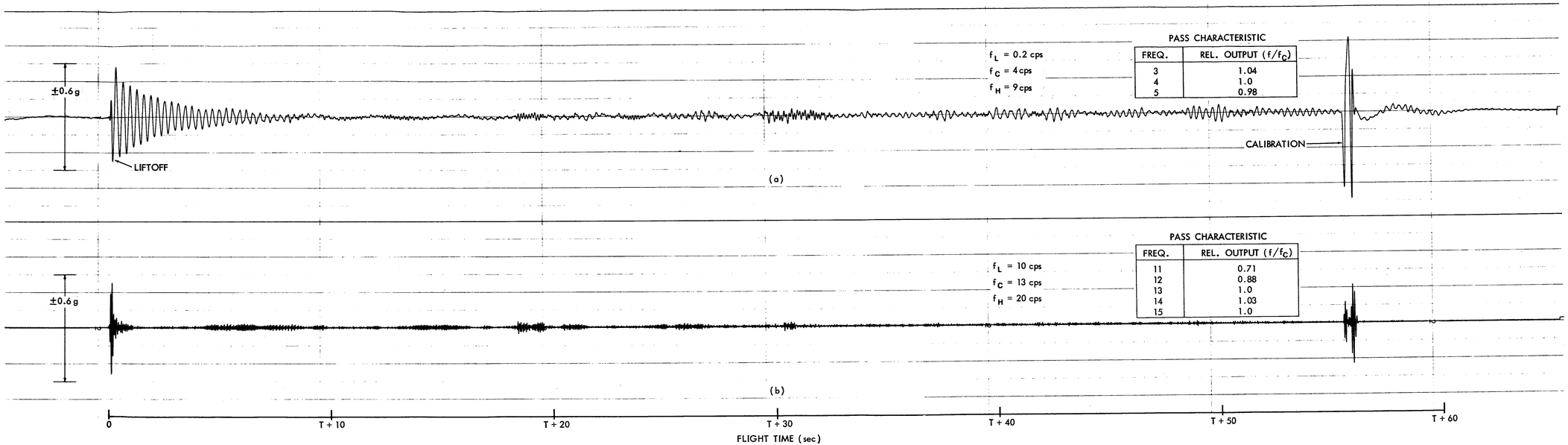

Figure 29–First-stage vibrations, narrow-band filtered. (a) Signal of the 3.5-cps vibration; (b) signal of the 13-cps vibration.

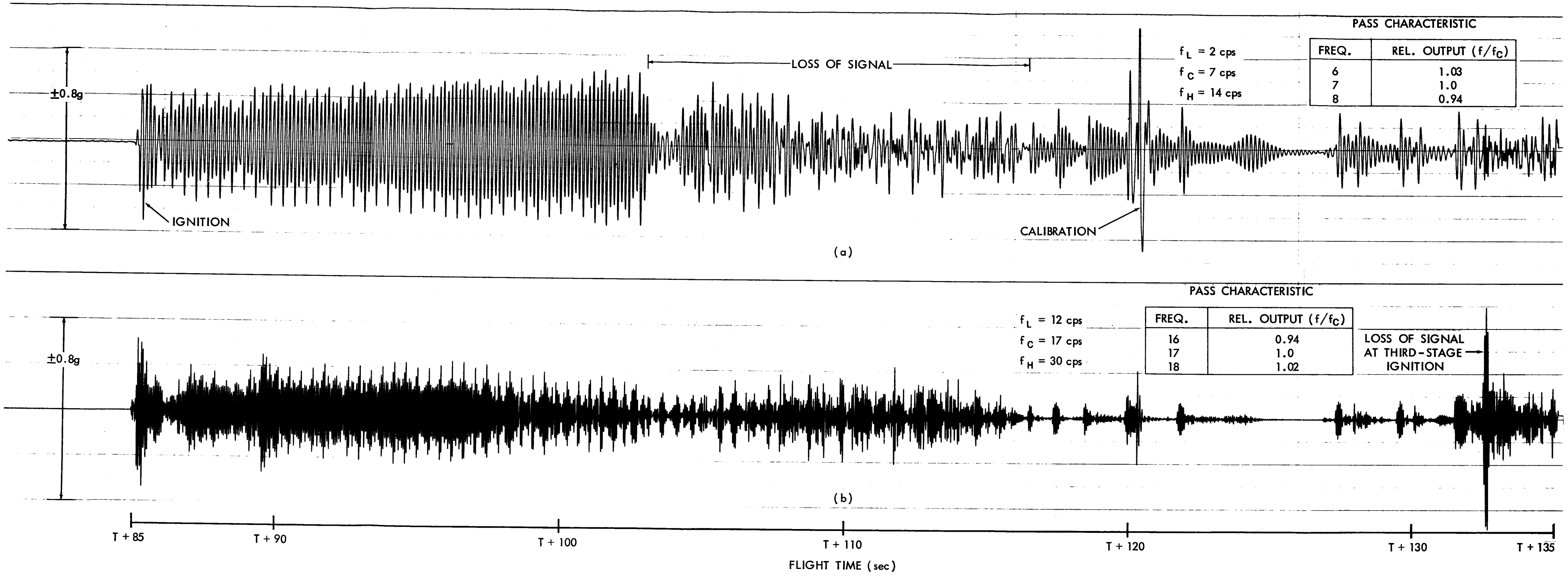

Figure 30–Second-stage vibrations, narrow-band filtered. (a) Signal of the 7.5-cps vibrations; (b) signal of the 17-cps vibration.

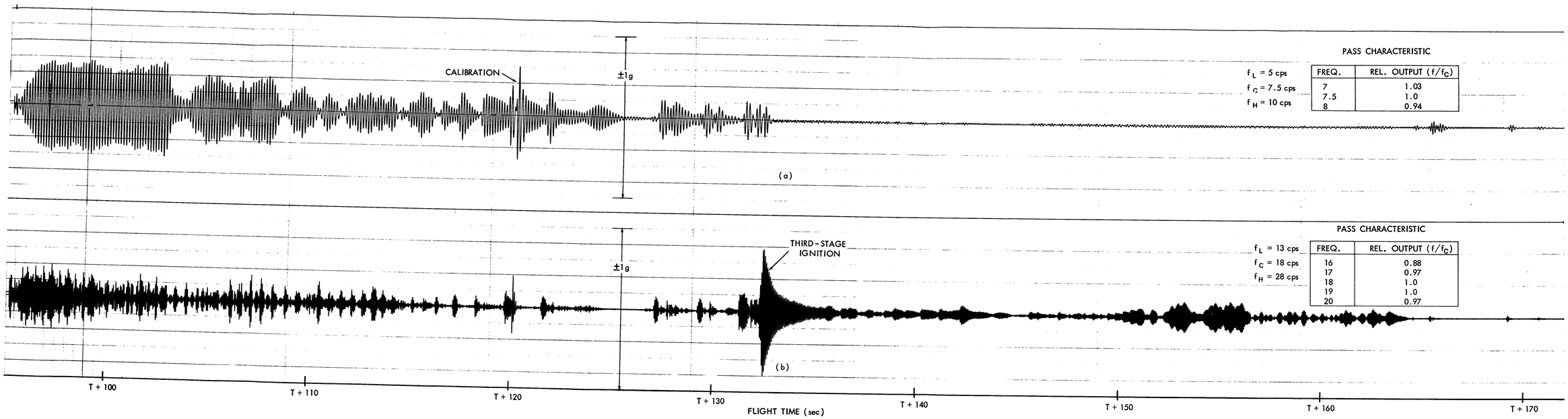

Figure 31–Second- and third-stage vibrations, narrow-band filtered. (a) Signal of the 7.5-cps vibration; (b) signal of the 16-20-cps vibration.

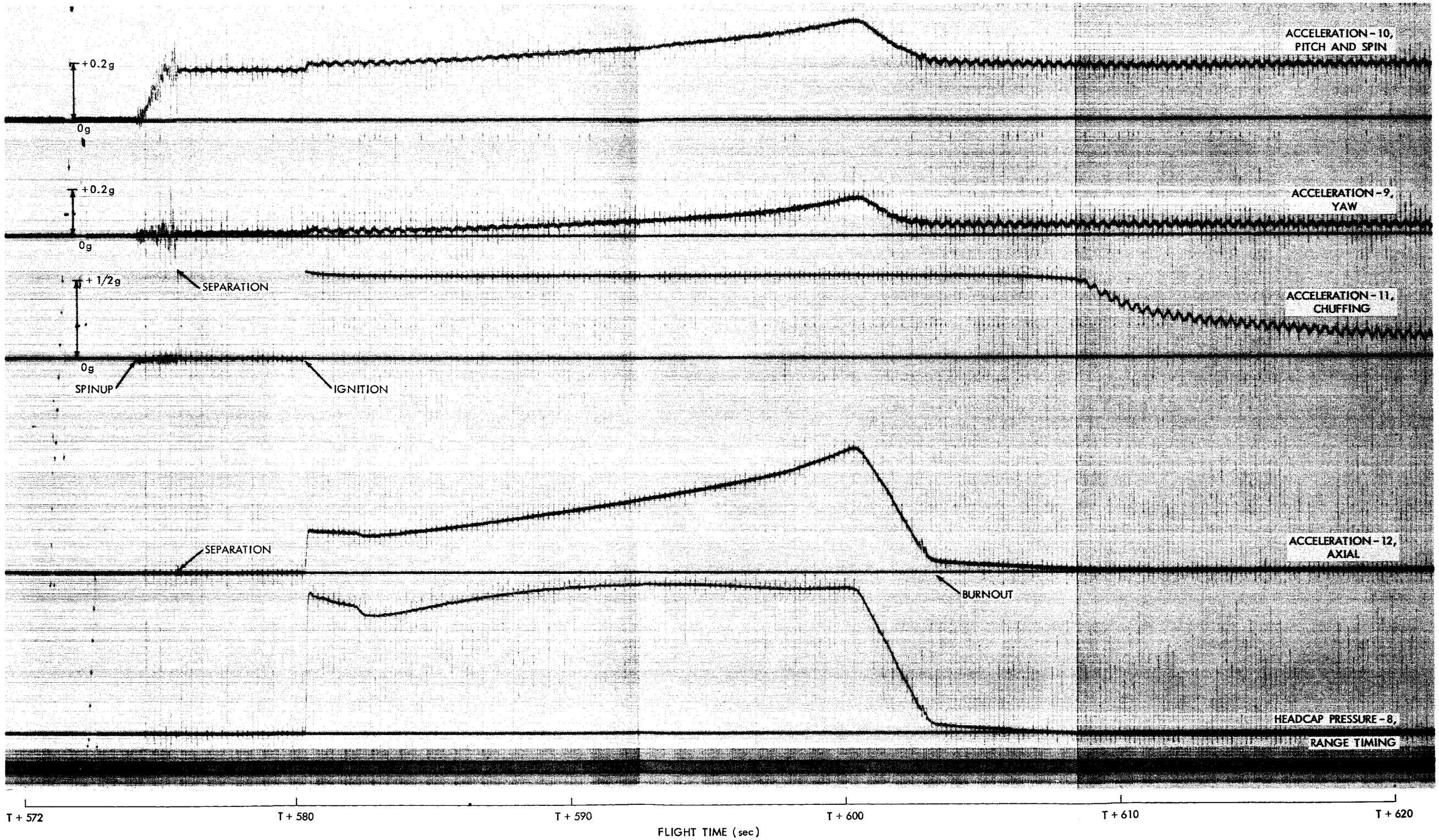

Figure 35—Fourth-stage real-time oscillograph record, acceleration and pressure.

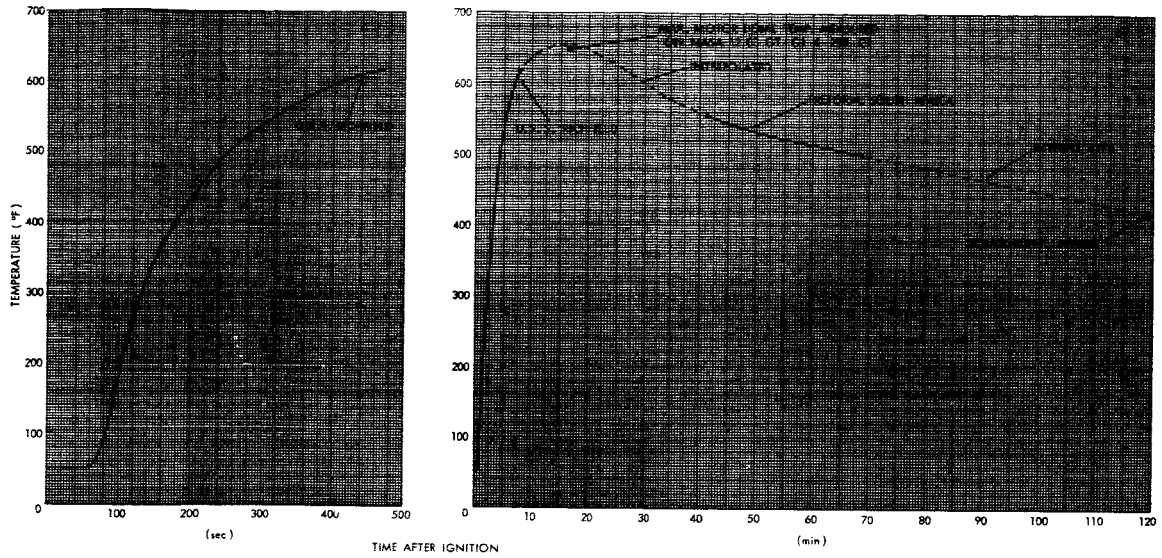

Figure 36–X-258 dome temperature.

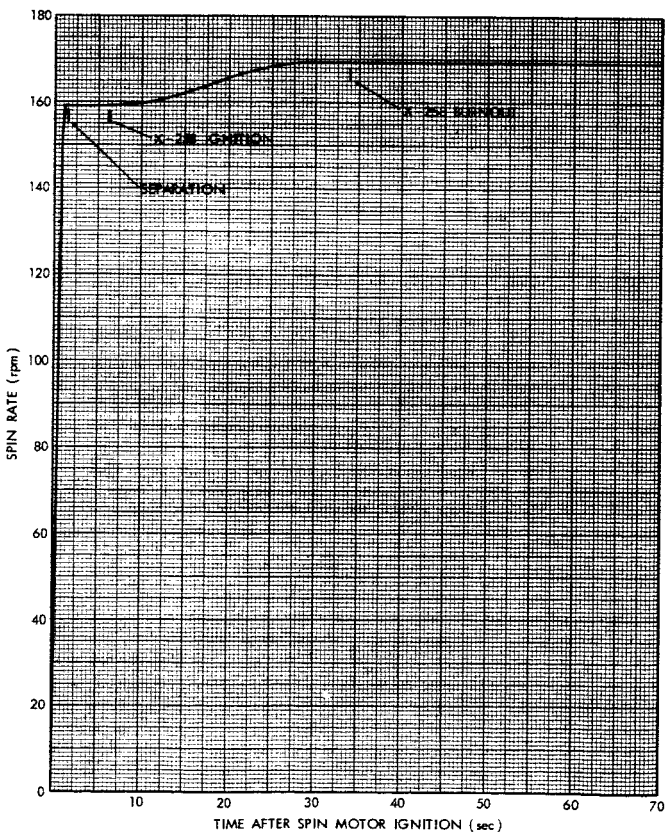

Figure 37–Spin-rate time history.

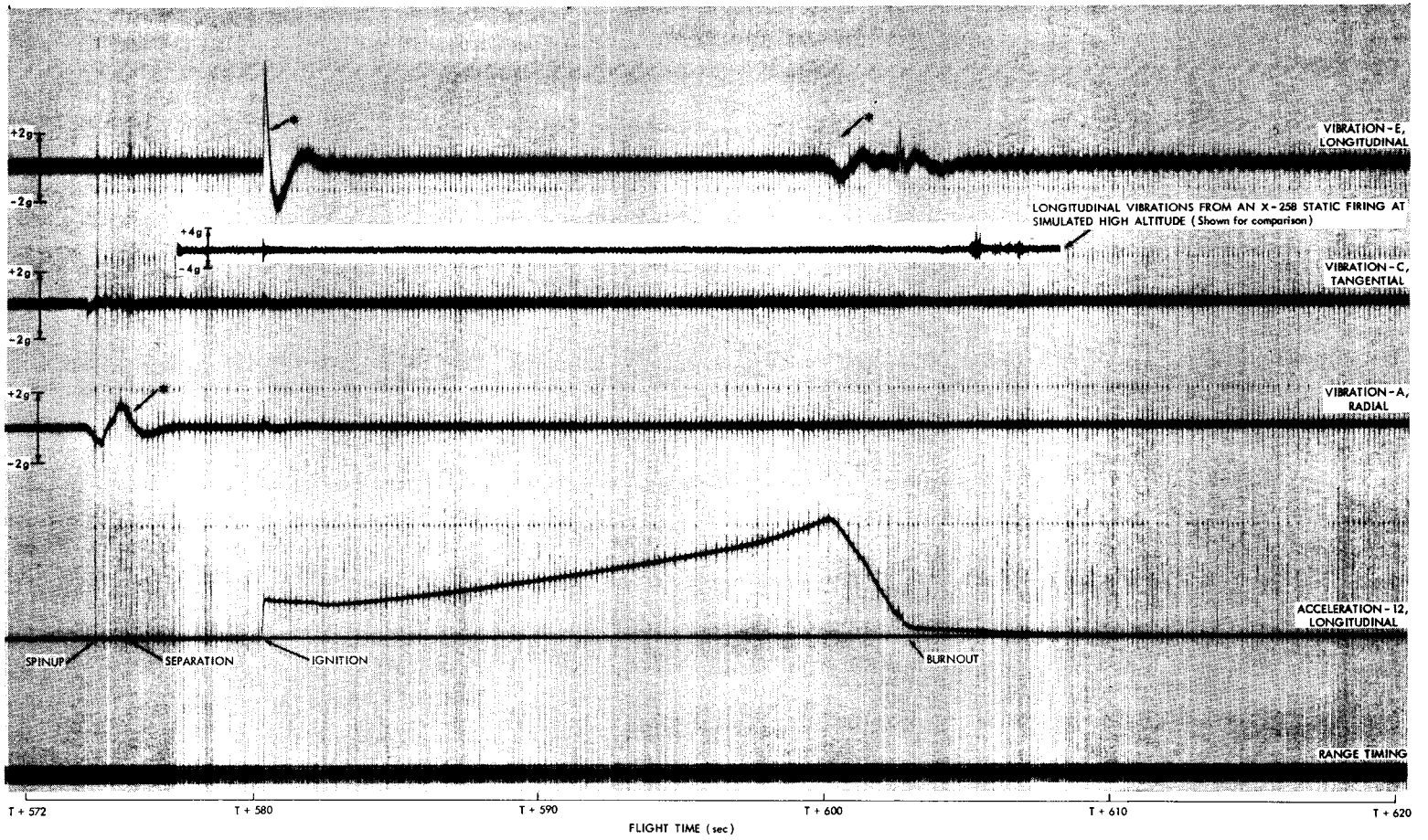

* Result of AC-coupled accelerometer system attempting to follow a steady acceleration.

Figure 38—Fourth-stage real-time oscillograph record, acceleration and vibration.

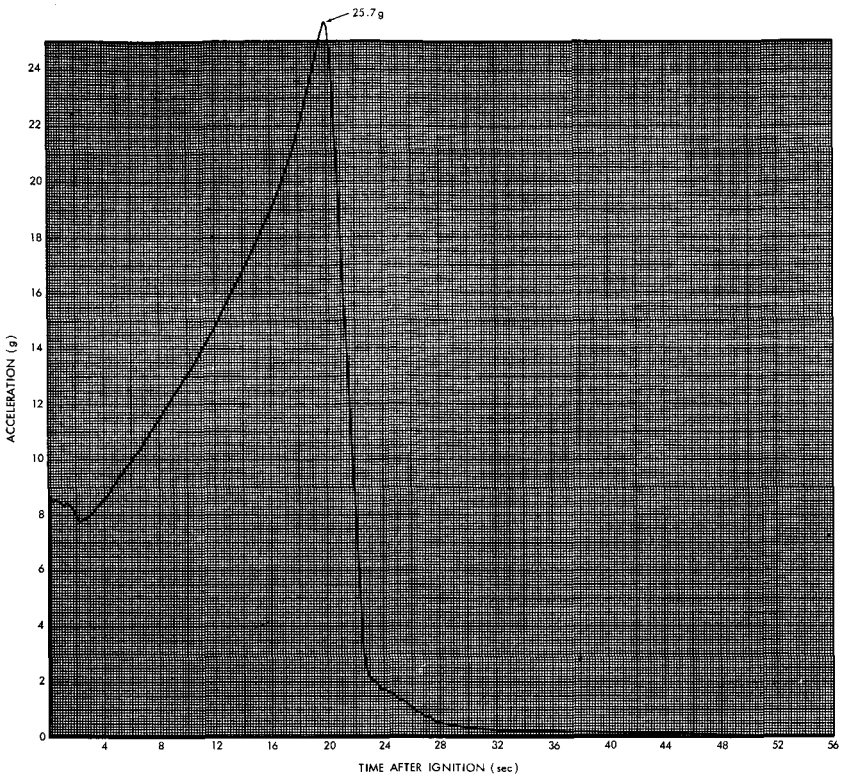

Figure 33–Fourth-stage steady acceleration time history.

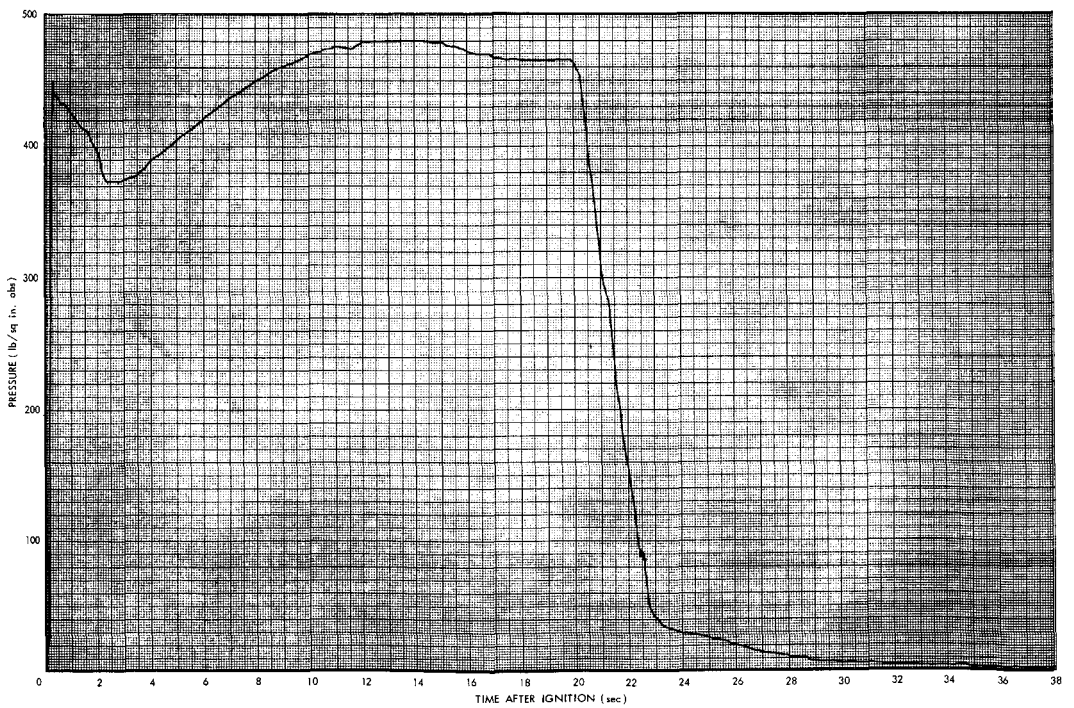

Figure 34–X-258 headcap pressure time history.